

The College of William and Mary

The Investigation of Radiation Detectors with Silicon Photomultiplier Readout

A thesis submitted in partial fulfillment of the requirement
for the degree of Bachelor of Science in Physics from
The College of William and Mary

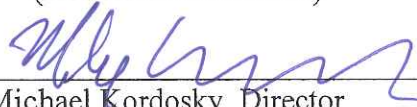
by


Matthew A. Loftus

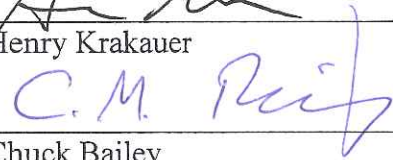
Accepted for

Honors

(Honors or no-Honors)


Dr. Michael Kordosky, Director


Dr. Henry Krakauer


Dr. Chuck Bailey

Williamsburg, VA
April 24, 2013

THE COLLEGE OF WILLIAM AND MARY

HONORS THESIS

DEPARTMENT OF PHYSICS

Investigation of Radiation Detectors with Silicon Photomultiplier Readout

A thesis submitted in partial fulfillment of the requirements for the degrees of Bachelor
of Science degree in Physics from the College of William and Mary

Advisor:

Author:

DR. MICHAEL KORDOSKY

MATTHEW LOFTUS

Senior Research Coordinator:

DR. HENRY KRAKAUER

May 5, 2013

Contents

1	Overview and Background	2
1.1	Purpose	2
1.2	Underlying Mechanisms and Devices: Scintillation and Photo-Detectors	3
1.3	SiPM Performance Studies	7
1.4	Physics Motivation: Particle Identification by Time of flight	9
2	Design and Construction	11
2.1	Test Setup	11
3	Performance Studies: Counting Efficiency	15
3.1	Coincidence Rate Measurements	16
4	The Wavelength Shifter	21
5	Performance Analysis: SiPM/Scintillator Output and Integrated Charge Spectra	28
5.1	Premise	28
5.2	Voltage Traces and Spectra	29
5.3	Analysis: Taking SiPM Dark Activity(no Scintillator present) into Account	35
6	Radioactive Source Test	37
7	Counter Efficiency: PMT Based Tests	38
7.1	Overview	38
7.2	Efficiency: Geometry 1	43
7.3	Efficiency: Geometry 2	45
7.4	Efficiency: Geometry 3	48
8	Conclusions	50
	References	53

1 Overview and Background

1.1 Purpose

The goal of this project is to investigate how efficiently scintillator radiation detectors function with silicon photomultiplier(SiPM) based readout. In recent years, faculty and staff at William and Mary built and assembled the hexagonal scintillator planes and associated electronics readout for the MINERvA neutrino experiment. The final product can be seen in figure 1.

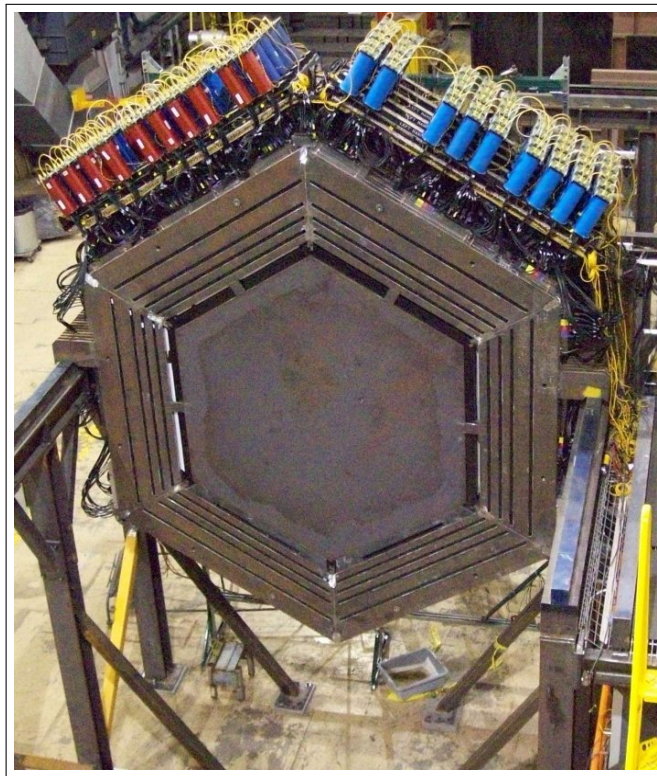


Figure 1: MINERvA Scintillator Detector with PMT Readout

The construction of these planes required gluing wavelength shifting fibers into each piece of scintillator and coupling them individually to a photo-detector known as a photomultiplier tube(PMT). This process was laborious, and required large input costs. With our investigation, we sought to determine whether or not this process could be simplified. More specifically, we wanted to know whether or not we could readout a plastic scintillator directly coupled to an SiPM, without wavelength shifting elements and complex gluing and coupling procedures. In conducting this study there were many fac-

tors we wanted to explore, including what the required size of the SiPM would be, how efficient were the SiPMs, and how that efficiency would change with the introduction of wavelength shifting fibers. We also wanted to explore what role noise played in SiPM operation, what the single photon sensitivity of the SiPMs was, and how it depends on the bias voltage.

In addition to their use in large-scale detectors, we also wanted to explore the viability of using SiPMs to build an application specific detector known as a time of flight counter. Our primary purpose in building time of flight counters is for particle identification in low energy test beams(300MeV/c-1000MeV/c). Test beams provide sub atomic particles of known momentum and identity which are used to calibrate detectors and detector elements for larger experiments. In characterizing test beams, it is important to accurately measure the flux of the different particles that make up the beam. In other words, experiments must determine what the beam is composed of and how much of each particle is present. One of the most important performance parameters of a TOF counter is known as the timing resolution, which is defined by how accurately the time at which a particle crossed the detector can be determined [9]. With a good timing resolution, a TOF counter can measure this distribution and give experimentalists important data about the performance of their beamline. In many high energy physics(HEP) experiments, wavelength shifting elements are often used in coupling scintillators to photo-detectors to improve detector performance. As stated before, we would like to determine how efficient direct coupling is, and whether or not wavelength shifting elements are necessary in SiPM-Scintillator detectors.

1.2 Underlying Mechanisms and Devices: Scintillation and Photo-Detectors

A typical time of flight counter consists of at least two scintillation devices, each of which is connected to one or more photo-detectors. Scintillation is a process inherent to certain organic and inorganic compounds, by which light of a characteristic spectrum is emitted from the medium following the absorption of radiation. When an energetic particle travels through the scintillator, it ionizes atoms in the base of the scintillator,

freeing electrons. These electrons then excite atoms in the fluor component of the scintillator, causing their electrons to move to a higher energy level. When the electrons in question return to their original state, the atoms emit photons, and thus particles passing through the scintillator with enough energy create large amounts of light. The scintillator we are using was manufactured at Fermilab for the MINOS and MINERvA experiments, and consists of rectangular extruded polystyrene bars covered in a coating of titanium dioxide paint, except on the front and back ends. Our scintillator utilized a polystyrene base, with two fluors known as PPO and POPOP, which act to increase the output light wavelength, shifting it from the ultra-violet to the blue portion of the electromagnetic spectrum [10].



Figure 2: Left: Plastic Scintillator w/ TIO_2 . Right: Light-Tighted Scintillator w/ WLS Fiber [9]

The plastic scintillator we used in our experiments is shown in figure 2. The titanium dioxide is totally internally reflective, and guides the scintillation light such that it may only exit from the front and back ends of the bar. Photo-detectors take many forms, but in the realm of particle physics research they are most commonly used to convert light into measurable electrical signals. They utilize the photoelectric effect, the process by which photoelectrons are produced when a photon strikes a conducting medium. The standard photo-detector of choice in recent decades in particle physics has been the photomultiplier tube, abbreviated PMT. A PMT consists of a cathode, multiple

dynodes, and an anode, all made with conducting materials. A typical PMT-Scintillator combination is depicted in figure 3.

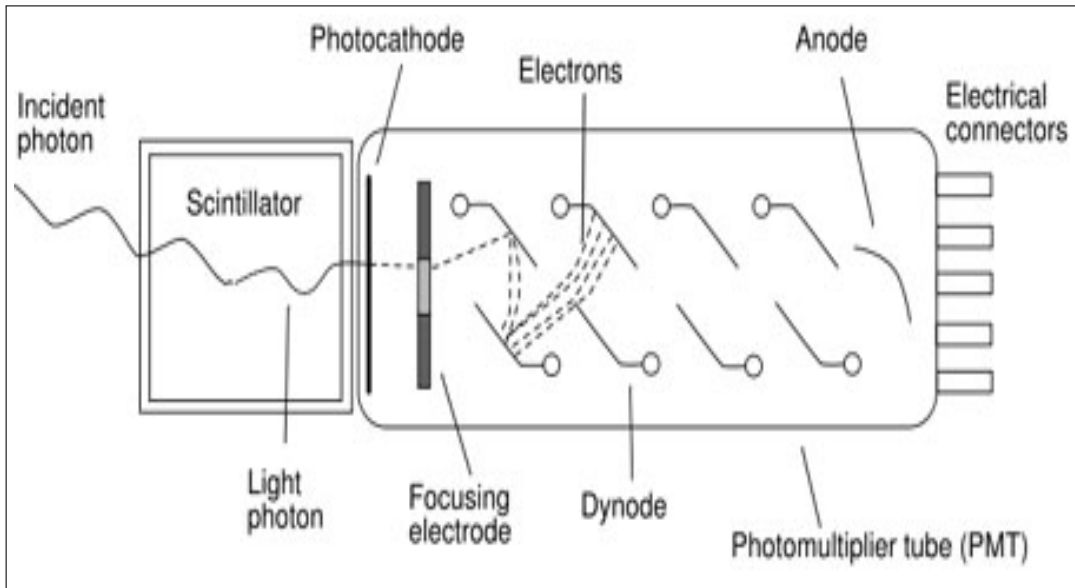


Figure 3: PMT-Scintillator Detector[5]

A voltage difference is applied between each stage of the PMT, and acts to accelerate electric charges and create an amplification of the electrical signal. When a photon strikes the photocathode of the PMT, a photoelectron is created, which is accelerated through a focusing electrode to the first dynode, where it knocks loose a greater number of electrons. This amplification process occurs between each dynode until the signal reaches the anode, contributing to the overall gain of the PMT. The gain of a photo-detector is the net amplification of the initial input signal. PMTs typically have a gain of around 10^6 [9]. From the anode the electrical signal is processed and analyzed, giving the experimenter valuable information about the original source of radiation. In detector applications, the cathode of the photo-detector is attached to one of the ends of the scintillator, so that when energetic particles travel through the scintillator, they create a light signal that may be recorded by the photo-detector, as shown in figure 3.

In recent years, a new photo-detector, called a silicon photomultiplier(SiPM), has been introduced with large success. SiPMs have demonstrated an advantage over PMTs in their size, their required power supplies, in their reaction to magnetic fields, and in other operational parameters. A SensL 10050 SiPM with a 1mm array and a

basic diagram showing its parts and operation are shown in figure 4.

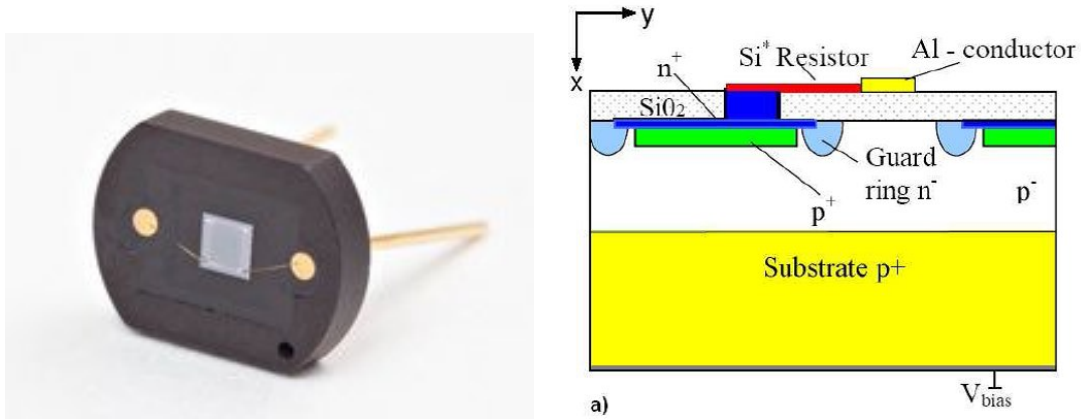


Figure 4: Left: SensL SiPM [11]. Right: SiPM Operation Diagram [5]

The mechanisms involved in SiPM operation are slightly different, but the photoelectric effect is still the fundamental element of its operation. SiPMs utilize the semiconductor silicon, and operate with only one stage of gain. The SiPM array consists of a large number of individual pixels which act in Geiger mode, meaning they are either on or off. When the light strikes the cathode, which is denoted in figure [5] by 'Si Resistor', a photoelectron is released into the silicon substrate. Like the PMT, a voltage difference is applied between the cathode and the anode, only in this case there are no dynodes present. At low voltages, the photoelectron will travel from the cathode to the anode without any amplification. However, when the voltage difference is increased to a large enough value, known as the breakdown voltage, a process known as avalanche multiplication occurs. In this process one or more photoelectrons are accelerated to a high enough velocity that they collide with atoms in the silicon layer, freeing a large number of electron-hole pairs, which in turn free an even greater number of electron-hole pairs. Electron-hole pairs refer to a an electron freed from an atomic lattice and the accompanying absence of an electron in the medium. The holes drift toward the cathode where they are discharged, while the electrons are drawn to the anode, where they provide the output electrical signal. Silicon is such that one stage of gain provides a comparable amplification to that of PMTs. Other advantages of SiPMs include their small size, low operating voltages, and resistance to magnetic fields [5]. For example, the SensL 10050

SiPM array we have used for our experiments has a breakdown voltage of 27.5 volts, while most typical PMTs require 1000 volts or more to function[3]. In detector and beamline experiments, strong magnetic fields are often present, especially when using magnetic spectrometers for particle momentum measurements. PMTs' performance are greatly impaired by magnetic fields [2], so SiPMs resistance to them provides a very practical benefit. For these reasons, we chose to investigate SiPMs. This required an initial analysis of the characteristics of our Sensl SiPMs to familiarize us with their operation, as all experiments we had previously conducted in light detection utilized PMTs.

1.3 SiPM Performance Studies

During the summer of 2012, I was able to to perform an in depth study of our SiPM arrays. We had recently acquired six SiPMs, consisting of three 1mm arrays(10050 model), and three 3mm arrays(30035 model). For our study, we focused on the 1mm arrays, measuring a number of different parameters. One of the most important parameters was the relationship between SiPM gain and the applied bias voltage. To measure the gain, we had to devise a scheme to determine the overall charge amplification. Noting that the initial charge for a event generated by a single photoelectron is simply that of an electron, $e = 1.6 \times 10^{-19}$ Coulombs, we had to find the corresponding charge given on the scope, and divide it by the elementary charge to get the gain. To do this we took the integrated charge of the SiPM voltage trace for each oscilloscope trigger, and recorded the values in a histogram. The voltage traces and the corresponding histogram, which we will call the integrated charge spectrum, are shown in figure 5.

In the histogram we note the different peaks, which are roughly the integrated charge values corresponding to single photoelectron events, double photoelectron events, etc., with the definition of the peaks decreasing as the number of photoelectrons increases. Seeking the charge created by a single photoelectron, we calculated the difference(V.s) between the 1 P.E. and 2 P.E. peaks, and then divided by the elementary charge to get the gain. Figure 6 shows our measured relationship between gain and bias voltage vs. that given by the SiPM datasheet.

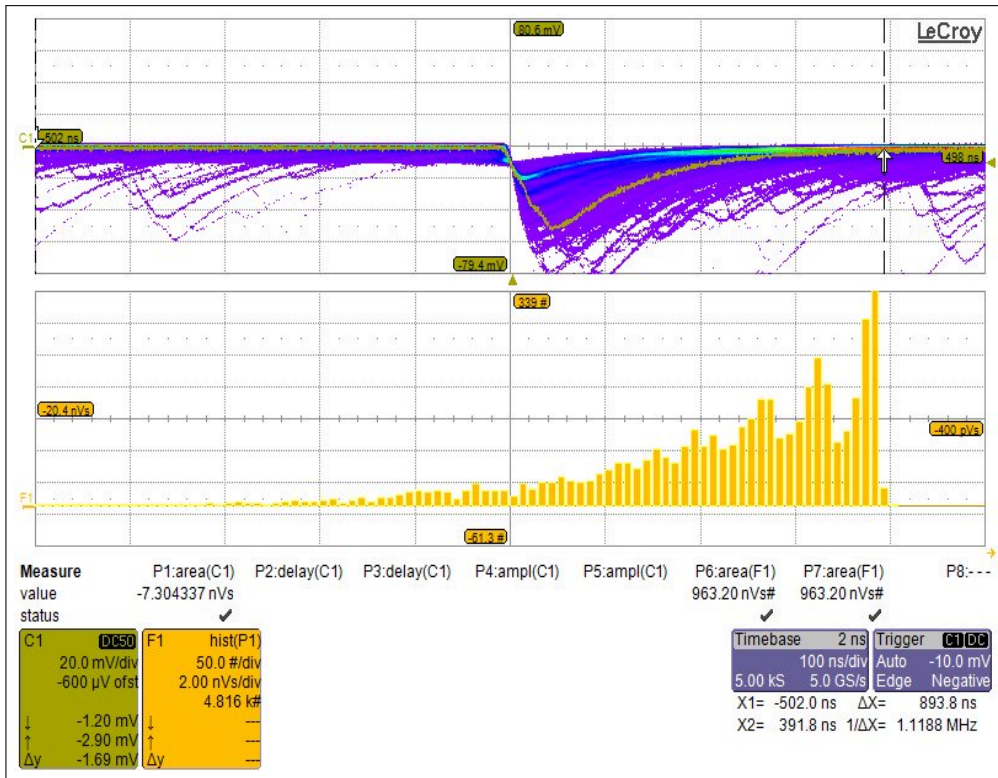


Figure 5: SiPM Voltage Traces and Integrated Charge Spectra

We note that the datasheet gain relationship is given as a function of the over voltage, the difference between the current bias voltage and the breakdown voltage. Here we extrapolated our results to find the bias voltage corresponding to a gain of zero, or the point at which avalanche breakdown occurs, and found our breakdown voltage to be 27.27 Volts, close to the value of 27.5 Volts given by the datasheet. Another important note is that our measured gain is approximately two orders of magnitude smaller than that given by the datasheet. This is indicative of a mistake in our experimental setup or a real discrepancy between the actual gain of our SiPMs and that given by the datasheets. We do note, however, that our gain does increase linearly with respect to our bias voltage, similar to the datasheet behavior.

Further, we studied the following relationships, dark current vs. bias voltage, dark count rate vs. bias voltage, and dark rate vs. threshold. For all of these studies, we found for each of the 1mm arrays, their performance agreed with that given by SensL [11]. With an understanding of the performance of our SiPMs, we determined that they would be suitable photo-detector candidates for our scintillator radiation detectors. In

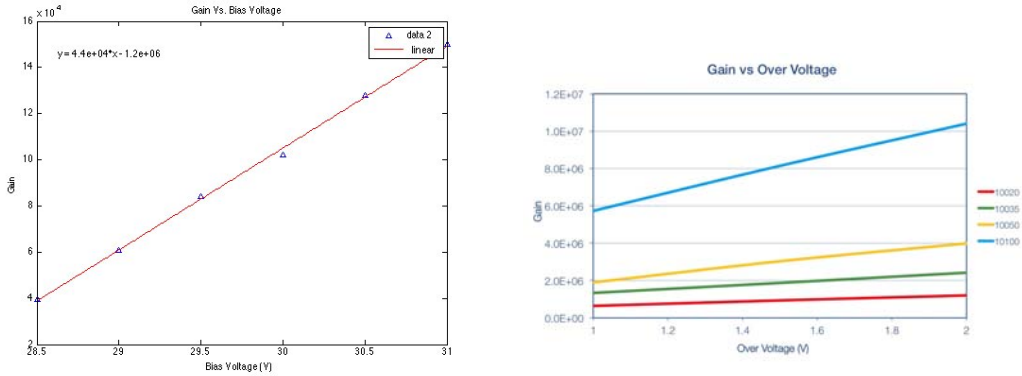


Figure 6: Left: Measured Gain. Right: SensL Datasheet Gain [11]

addition to studying the SiPMs' performance, these studies familiarized us with the tools and means of data acquisition we would be using throughout the following year in our detector analyses.

1.4 Physics Motivation: Particle Identification by Time of flight

As stated previously, a typical time of flight system consists of at least two scintillation devices, each with at least one photo-detector coupled to it. To explain the main principles, I will use the example of a 2 piece horizontal time of flight counter in a test beam setup. Here each scintillator will have one SiPM coupled to the front end. When an particle travels through the scintillator, the SiPM records the amplitude of the event as well as the time at which it occurred. In a test beam time of flight system, the two scintillator pieces would be placed on the beam axis, perpendicular to the direction of beam flux, and we would fix the distance between the two bars. The horizontal orientation coincident with the beamline axis is used so that the majority of particles that pass through the first scintillator will also pass through the second scintillator. We may determine the amount of time elapsed between a particle passing through the front and back scintillator pieces by studying the signals coming out of them. With the time and distance measured, we may determine the particle's velocity from the standard equation:

$$v = \frac{d}{t} \quad (1)$$

In experiments involving test beams, as mentioned above, magnetic spectrometers are utilized independently of TOF counters to measure the momentum of particles in the beam. The relativistic equation relating the momentum and velocity of fast-moving particles is:

$$p = \gamma m v \tag{2}$$

Where p is the momentum, v the velocity, m the rest mass, and γ the relativistic constant of the particle in question. Hence with independent measurements of the momentum and velocity of a particle, we may calculate its rest mass. Noting that $\gamma = \frac{1}{\sqrt{1-(\frac{v}{c})^2}}$, and plugging equation 1 into equation 2, we come to the following result

$$m = \frac{pt}{d\sqrt{1 - (\frac{d}{ct})^2}} \tag{3}$$

Where d is the baseline separation between the two detector elements, c is the speed of light, and t is the time of flight. The remaining parameters are defined above. As the masses of most elementary particles are known with reasonable certainty, determining the rest mass of a particle is the primary means of particle identification. Hence by measuring the masses of particles in a test beam, we may determine the particle content.

Figure 7 shows the mass distribution for the test beam used by the MINERvA neutrino experiment. Here the peaks of the curve correspond to masses of the different particles present, with the names of the particles listed directly above the x-axis. Here we see we have a significant flux of pions, kaons, protons, and alpha particles, with pions and protons accounting for most of the events. A pion is a meson which has a mass approximately 270 times that of an electron. The width of the peaks is determined by the timing resolution of the detector elements, with a higher resolution leading to narrower peaks and subsequently more accurate particle distributions. Another plot from the MINERvA experiment relating particle momentum and time of flight is given in figure 8 .

Here the different bands correspond to the different particles shown in figure 7. With a good timing resolution, the bands are narrower and again, knowledge of the

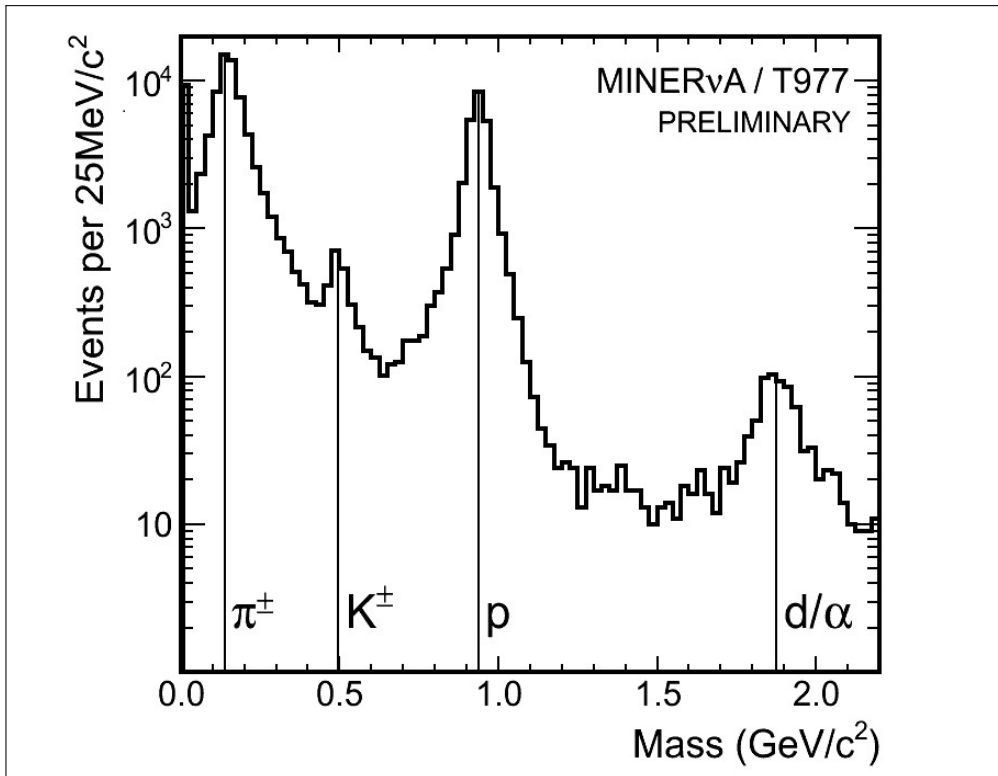


Figure 7: Mass Spectrum Example[1]

particle fluxes become more accurate. In our TOF system, the baseline (the separation between the two detector elements) is always less than half of a meter. Subsequently, our system is technically a test stand, as it can measure detector performance characteristics but cannot effectively identify particles due to its short baseline and our lack of an independent system to measure particle momentum. In the following sections, I will describe the original design of our TOF counter and the subsequent modifications that took place over the course of the year.

2 Design and Construction

2.1 Test Setup

Figure 9 shows the original schematic for the setup of the detector. When starting construction, the most important thing to establish was the basic structure of the detector, and to ensure that it had significant flexibility in its design so that modifications

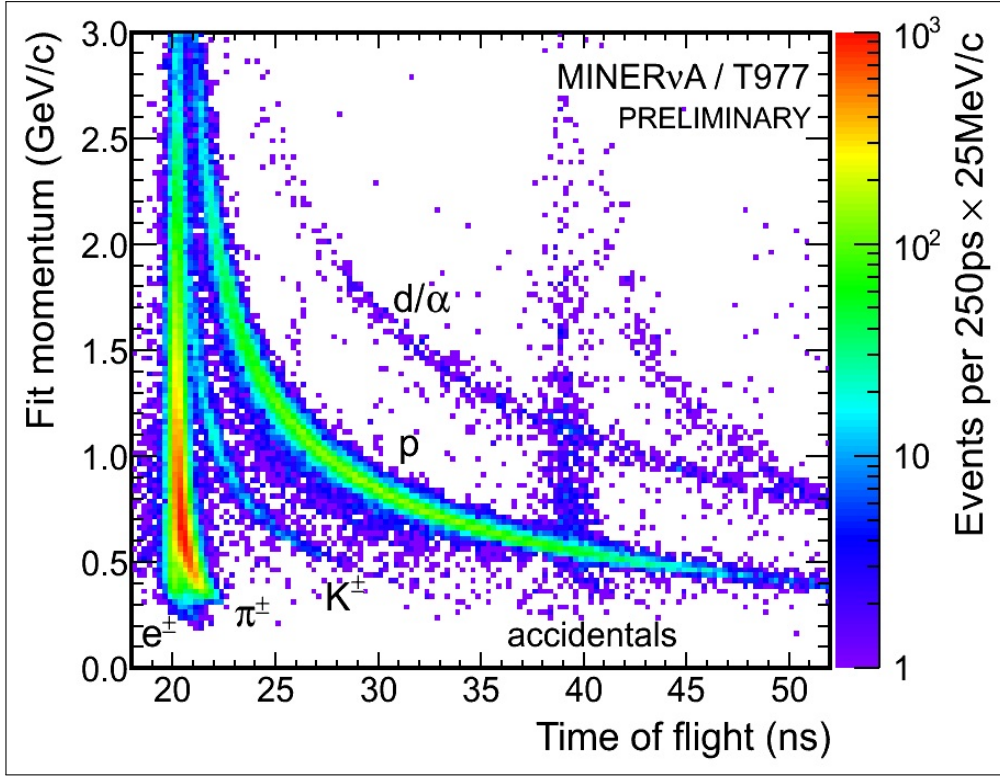


Figure 8: Particle Momentum Vs. Time of Flight[1]

could be implemented without needing to alter the major parts of the apparatus. The most important initial considerations included secure and independent clamping of each of the elements, the ability to couple and uncouple the scintillator/SiPM without losing their horizontal and vertical position in relation to each other, and the ability to change the vertical separation between the two scintillators and lock them in position when desired. From the initial design in figure 9, we can discuss the structure of the counter. The original design consists of the two scintillator bars, each coupled to one SiPM/EVB combination. The EVB is the electrical housing which connects to the anode/cathode of the SiPM and contains the amplification and voltage biasing circuits. Power is supplied through a port on the EVB. It also contains the SMA output port which transfers the SiPM output to an data acquisition system, typically the oscilloscope in our experiments. We note that in the actual experimental setup, there was no air gap between the end of the scintillator and the face of the SiPM array as is depicted in Figure 9. The actual experimental apparatus is displayed in figure 10.

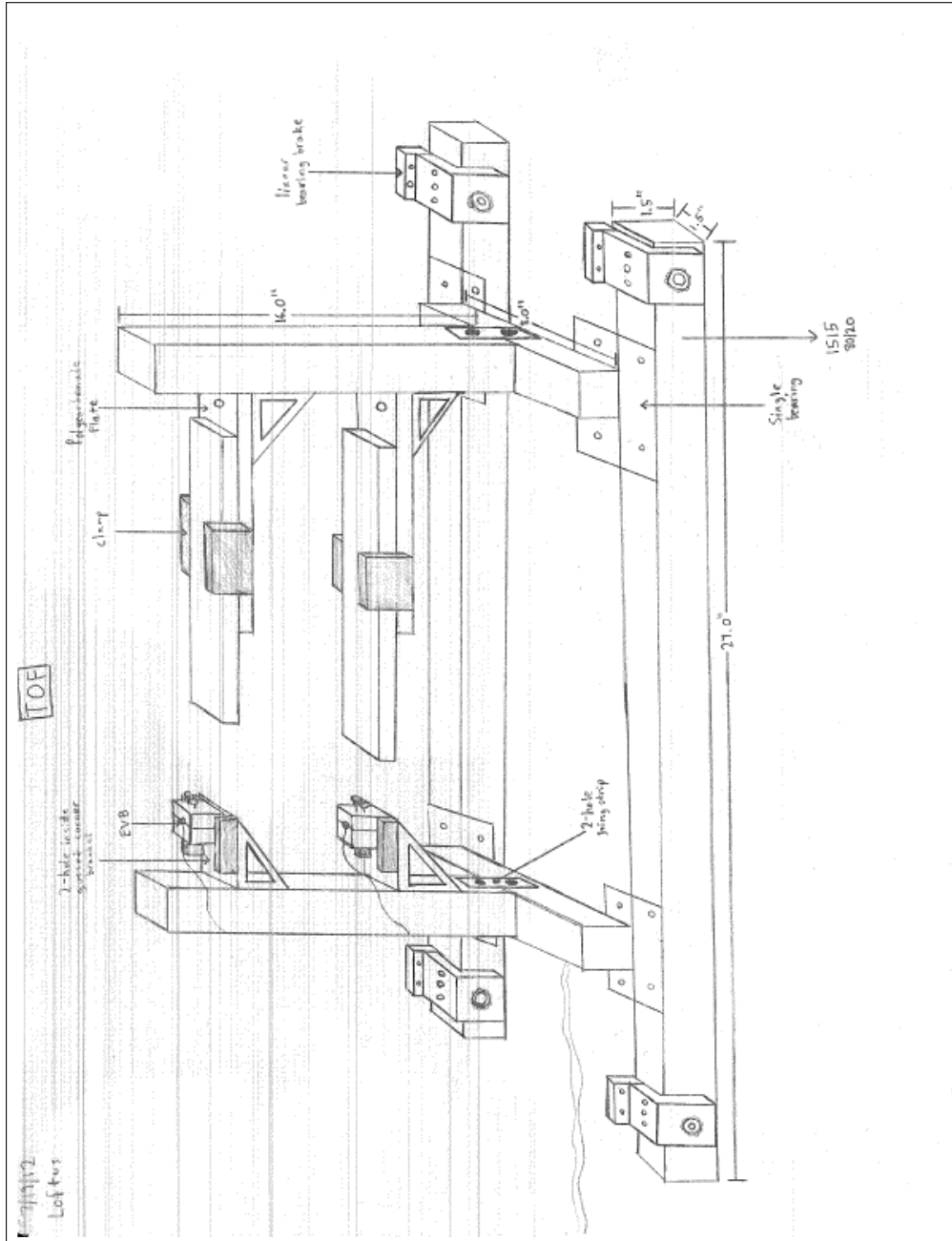


Figure 9: Original detector design

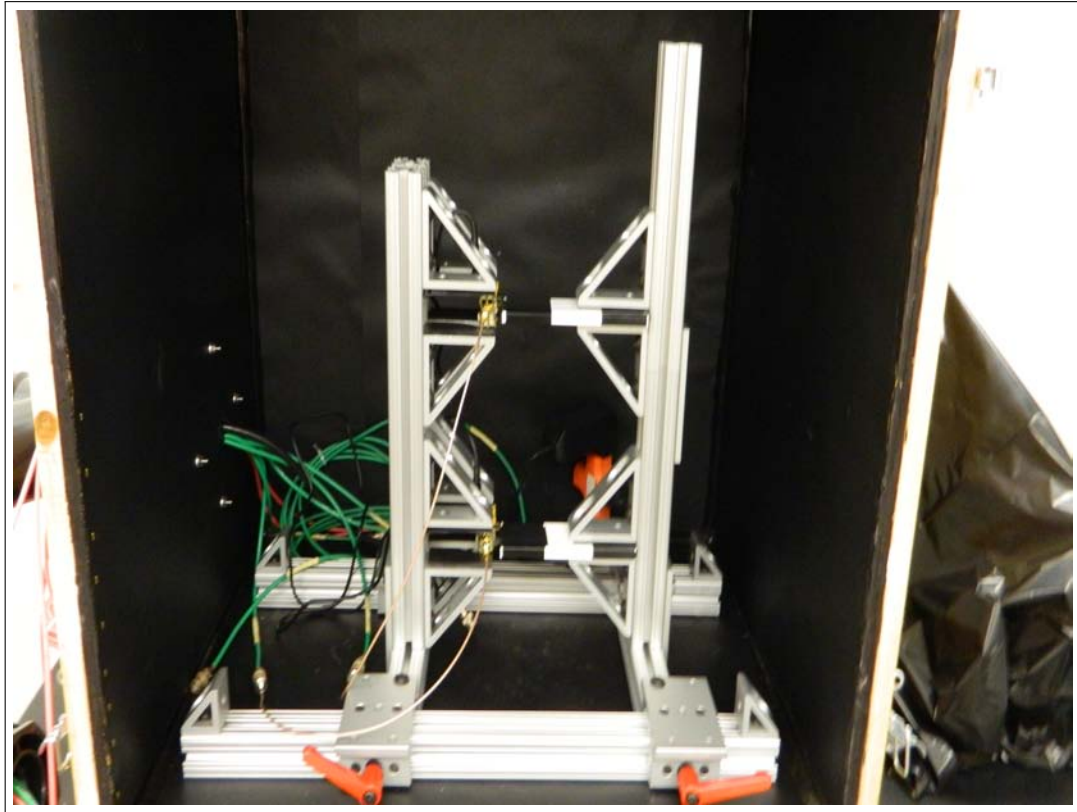


Figure 10: First Prototype

For the first build, I constructed the frame using 80-20 stock. I assembled it such that the two main vertical posts could move back and forth on the two base rails to ensure precise coupling. Also note the two red handled mechanisms in the foreground of figure 10, which provided a lockout capability for the two vertical posts when the desired separation was achieved. In addition, the triangular components on inward sides of the vertical rails, which serve as the detector platforms, had vertical mobility so that the separation between the two scintillators could be adjusted and locked with relative ease. Due to the nature of 80-20 and the abundance of compatible accessories, we had freedom to make changes to the detector, which would prove to be essential in the coming months. Another important aspect of the apparatus is the light tight enclosure our counter occupancy. This enclosure, referred to as a dark box, serves to prevent ambient light from reaching the apparatus and adversely affecting the output. When ambient light hits the array, it creates large amounts of noise and effectively restricts us from taking any useful data, due to the fact that the SiPM pixels are constantly firing in

response to the light.

In assembling the detector, modifications were required, but we were able to maintain the original structure we had in mind. For this version of the detector, I used $5 \times 1 \times 10$ cm rectangular polystyrene bars. I attached a highly reflective material to the back end so that light would reflect towards the SiPM and not escape from the back end. I used the reflective material on the front end as well, only in this case leaving a small square of uncoated polystyrene exposed, just large enough cover the face of the SiPM array. Also, we note the black tape, which in later versions covers the whole scintillator bar, acting to prevent unwanted light from entering. We currently possess multiple 1mm and 3mm SiPM arrays, where the dimension corresponds to the length of the square sides of the silicon/cathode face. However, we also only possess one EVB for each type of array. This has disadvantages, as the 3mm array has completely different performance characteristics than the 1mm array, including gain properties and single photon resolution. Nonetheless, we compensated for these disadvantages in subsequent experiments by adding an extra stage of amplification to the output of the 3mm SiPM to match the overall gains of the two detector elements.

3 Performance Studies: Counting Efficiency

To study the performance of our original setup we conducted a measurement of the coincidence rate between the two scintillator bars. Output voltage studies and integrated charge distributions are very valuable in gauging the efficiency of photo-detector-scintillator experiments, but at this point our method of coupling was not optimal, so we did not study these in depth at that stage. With no coupling medium between the face of the scintillator and that of the SiPM, we experienced significant light loss due to reflection off of the interface caused by the differences in the indices of refraction of polystyrene and silicon. Ultimately we acquired Bicon B-600 optical grease, which acts to match the indices of refraction and minimize light loss, to couple the two components together. Throughout the rest of the project, we utilized integrated charge spectra and output voltage amplitudes to determine the effectiveness of our setup. At this stage

however, we relied on the coincidence rate measurements for a benchmark of our TOF counter's performance.

3.1 Coincidence Rate Measurements

In test beam applications, the two elements of a time of flight counter are often separated by a distance on the order of meters to gain a useful time differences between events in the respective scintillators. The minimum separation they can have while still gaining useful measurements is determined by the timing resolution of the counter. In our case, however, we kept the distance between the two scintillators less than 20cm. This was because the size of our light-tight enclosure and 80-20 stock put a low upper limit on that separation, but also because coincidence measurements are easier to perform at a small separation, and yield important information about the efficiency of the scintillators being used. In calibrating the detector initially, we utilized the abundance of minimum ionizing particles(MIPs) at sea level. MIPs are created in a process beginning with the reactions of protons and heavier nuclei in the upper atmosphere as they travel down towards earth. These nuclear interactions create π mesons, which then decay into muons, particles akin to a heavy electron. While muons have a half life of $2\mu s$, due to their high velocity and relativistic effects, their lifetime is actually long compared to other elementary particles. As a result, muons are the primary source of MIPs at sea level, and a significant proportion of these travel vertically downwards. As MIPs travel near the speed of light, if they travel through our detector, we expect them to create events in the two scintillators at essentially the same time, separated by at most on 1-2 nanoseconds. Also, due to the nature of MIPs, they create large amounts of scintillation light, hence when an MIP goes through our scintillator we expect multiple SiPM pixels to be fired, creating a signal with a large amplitude. The thermal electrons that create the noise are randomly generated in the cathode of a single pixel, hence the corresponding amplitude has a small amplitude compared to that of MIPs. Thus we classified coincidences by large amplitude events occurring at nearly the exact same time. Now for vertical muons of energies greater than $1\text{GeV}/c$, the intensity at sea level

has been experimentally determined to be $I = \frac{1\text{muon}}{\text{cm}^2\text{min}^2}$ for horizontal detectors [4]. Thus taking the vertical cross-sectional area of our scintillator strip and multiplying it by the intensity given above, we estimate that our scintillator should observe 65 muons/minute, a rate slightly greater than 1Hz.

To experimentally measure this rate of coincidence in our counter, we used the NIM electronics units in our lab, which consisted of amplifiers, discriminators, coincidence counters, power supplies, and other DAQ units. Our test setup is shown in figure 11.

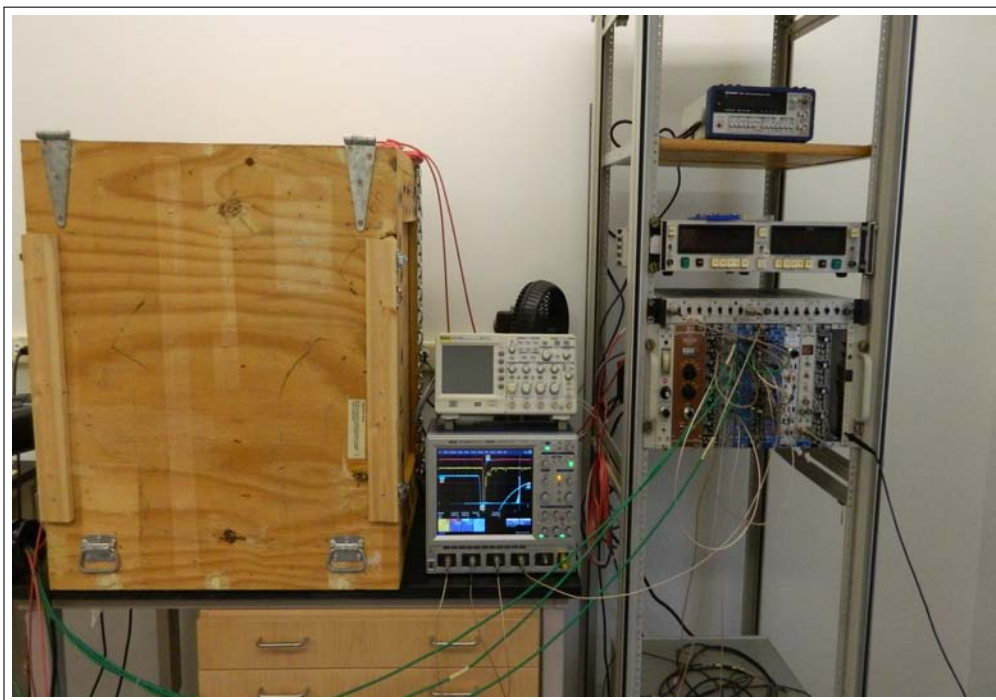


Figure 11: Test Setup

In the test setup, we see our dark box located on the left hand side, our oscilloscope in the center, and our NIM electronics modules on the far right.

In figure 12 we see the NIM electronics setup in greater detail. The individual modules described above are the rectangular units seen in the figure, with relevant units placed alongside each other for ease and clarity of electrical connections. First, I connected each of the two SiPMs to an individual channel on the **discriminator module**, which creates a logic pulse of adjustable width each time it receives a signal above a certain threshold. The thresholds and pulse widths could be set and adjusted

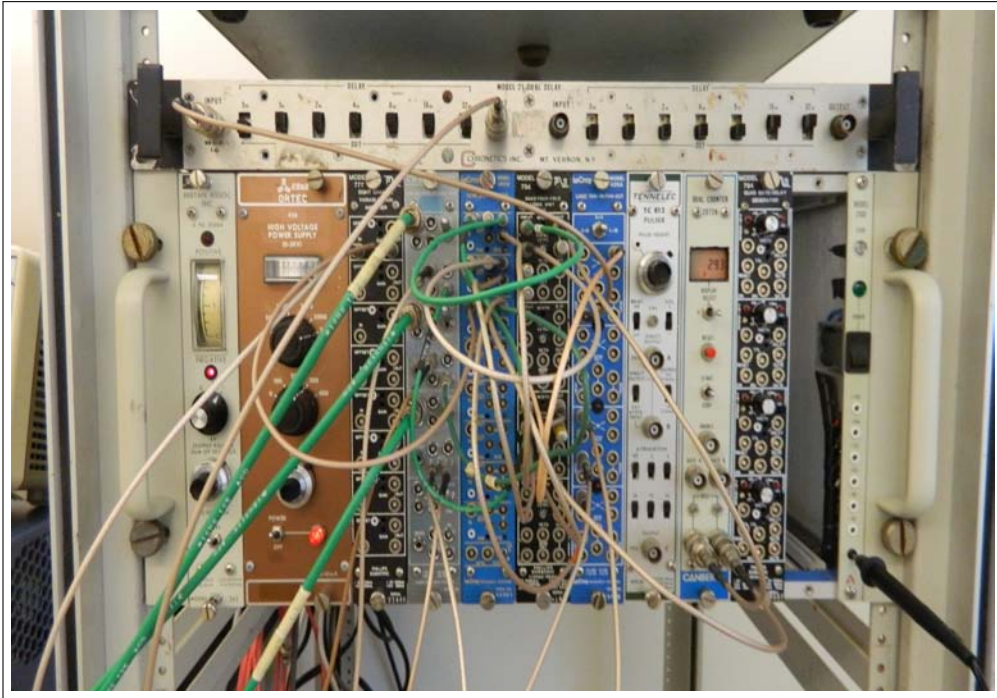


Figure 12: NIM Electronics Close-up

for each of the channels on the discriminator, which proves useful for example if one wanted to set a lower threshold for an input signal which had a lower initial amplification compared to other input signals. I then connected the 1mm SiPM to the first discriminator channel(D_1), and the the 3mm SiPM to second discriminator channel(D_2). The two discriminators were then in turn connected to the inputs of a single channel on the **coincidence module**. The coincidence module fires a logical pulse each time two of its inputs are in the logical high state at the same time. Hence if the discriminators fire at a similar time and their output pulses overlap in the coincidence module, the coincidence unit will in turn fire a logical pulse. Lastly, I connected the coincidence unit to an analog counter, which counted the number of coincidences in our scintillators. The logical elements of our experiment are summarized below.

Based on its logical operations, the coincidence unit can actually measure many different quantities, including the overall coincidence rate as well as the event rates(Hz) in each of the scintillators independent of the other. This hinges on the "and/or" function of the unit. In the "and" setting, the unit will only fire a pulse if both inputs go are low at the same time, so this is what measures the overall coincidence rate. In the "or"

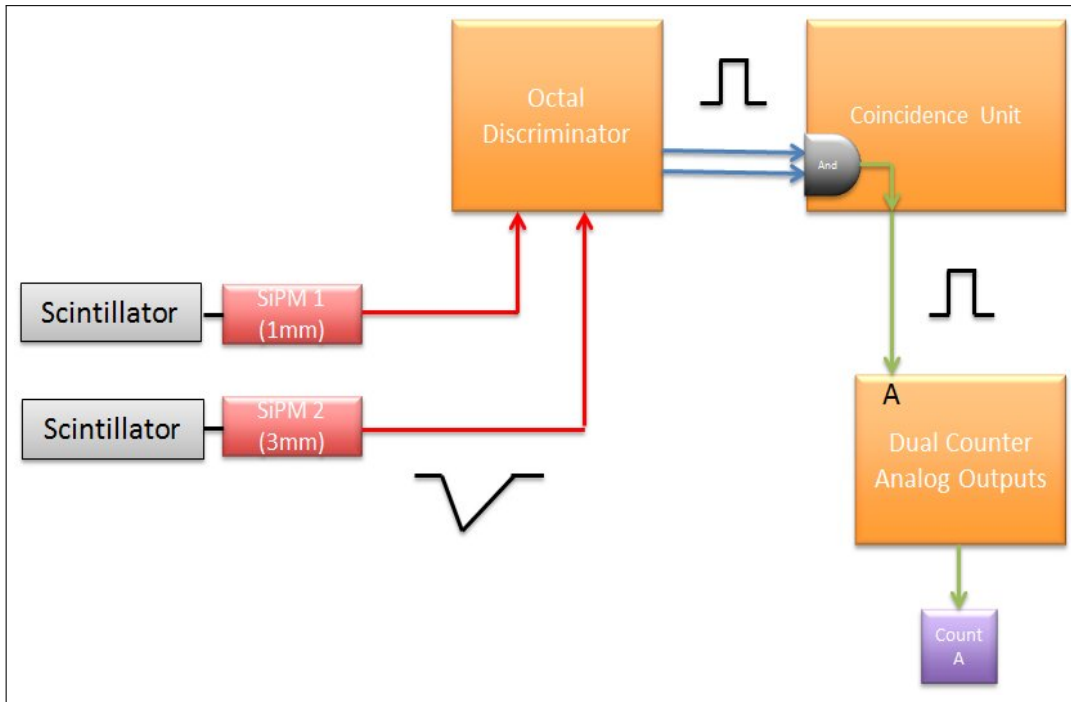


Figure 13: Counting Efficiency: Logical Elements

setting, the unit fires if either one or both of the inputs go low, hence if we disconnect one of the inputs in this setting, the counter will measure the independent event rate of the other input.

Each element of the TOF counter will have its own independent event rate, which means each discriminator output will inevitably be in the 'low' state for a certain fraction of each second. The significance of this is that false coincidences will occur, based on the fact that each element has its own independent rate and the fact that the NIM units output pulses of nonzero width. To determine these independent rates, let us take D_1 , for example. If we multiply the output pulse width of D_1 by the event rate (events per second) coming from D_1 , we will yield the fraction of each second that D_1 is in the 'low' state. Now as D_1 and D_2 both have their own rates, there is a significant probability that they will both be in the 'low' state simultaneously, resulting in a false coincidence. To measure this quantity I set the NIM unit's parameters as follows: $\text{Pulse Width}_{D_1} = 61.00\text{ns}$, $\text{Pulse Width}_{D_2} = 64.00\text{ns}$, $\text{Threshold}_{D_1} = 31.45\text{mV}$, $\text{Threshold}_{D_2} = 31.23\text{mV}$, $V_{\text{Bias}}(1\text{mm}) = 29.99\text{V}$, and $V_{\text{Bias}}(3\text{mm}) = 30.01\text{V}$. From the above discussion, we see that we must multiply the fractional time per second one of the dis-

criminators is firing times the independent event rate of the other discriminator (and vice versa), yielding the following formula for the rate of false coincidences per second (in Hz):

$$R_{fc} = PW_{D_1} * R_{D_1} * R_{D_2} \quad (4)$$

Where R_{fc} is the false coincidence rate (Hz), PW_{D_1} the width of the output logic pulse from D_1 in seconds, and R_{D_1}, R_{D_2} the independent event rates of D_1 and D_2 , respectively, measured in Hz. Prior to our coincidence test, we measured R_{D_1}, R_{D_2} , finding $R_{D_1} = 6.39 \times 10^4 \text{Hz}$ and $R_{D_2} = 0.654 \text{Hz}$. Using our false coincidence rate formula, we calculated the expected value to be $R_{fc} = 2.7 * 10^{-3} \text{Hz}$. Extrapolating R_{fc} to find the expected number of false coincidences in 1 hour yielded a value of 9.72. Extrapolating our expected rate of muon flux at sea level over the vertical cross-sectional area of our scintillator (65/min) yielded an expected value of 3900 muons/hour. Subsequently we performed an overall coincidence measurement over the course of an hour, yielding 10 total coincidences. This indicates a low efficiency. A likely cause was that we may not have been operating the 3mm SiPM in a sufficiently sensitive way, as indicated by the extremely low event rate R_{D_2} . After confirming that we were not operating the 3mm SiPM optimally, we set out to investigate the efficiency in a controlled way. We began by looking at the photon detection efficiency vs. wavelength characteristics of our SiPMs. The photon detection efficiency is a measure of how well input light is converted into an electrical signal, as well as what proportion of that light is detected. Figure 14 shows the photon detection efficiency, for a number of different SensL SiPMs, where the performance of our 10050 SiPM array is given by the yellow curve. We see from the figure that the maximum PDE occurs at approximately 500nm, meaning the most efficient signal amplification occurs when light with $\lambda = 500 \text{nm}$ strikes the cathode. At this value the PDE is slightly greater than 20 percent.

Our polystyrene scintillator's output characteristics and some related quantities are shown in figure 15. The 1%PPO+0.03%POPOP transmittance, given by the blue curve, shows the wavelength of the light created within our scintillator. Note PPO and POPOP are the dopants used in the polystyrene to create the scintillation mechanism. The curve shows that most of the scintillator's output light has a wavelength between

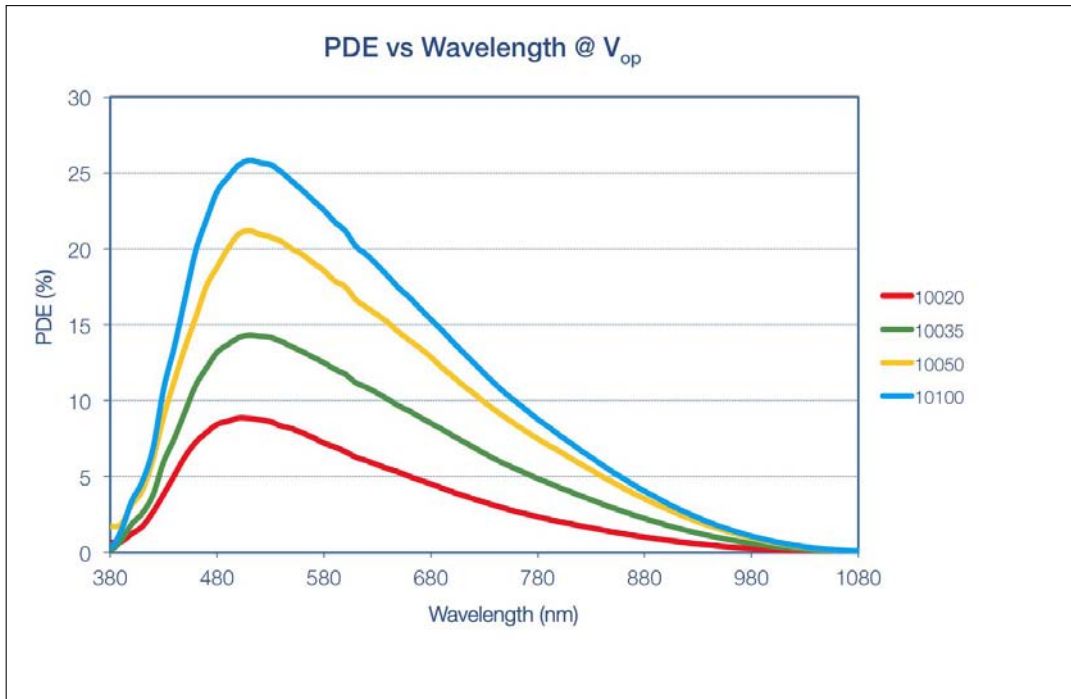


Figure 14: SensL SiPM PDE Characteristics [11]

400-420nm. Referring back to figure 5, we see that the 400-420nm region corresponds to a PDE of 5% or less, much lower than the maximum PDE for the 10050 SiPM. So the two media are not well matched optically, and much of the scintillator light is transmitted inefficiently. With a better optical coupling, we would ideally get a much higher signal amplitude for MIP events in our scintillator, thus allowing us to raise the thresholds and better discern between noise and actual particle detection events. This finding led us to our next modification of the detector.

4 The Wavelength Shifter

Our previous results motivated us to construct a device which would shift the wavelength of our scintillator output to a wavelength more suitable for our SiPMs. In figure 15, we see the red curve corresponding to K27 transmittance. K27 is the dopant found in the green WLS fibers, which have been utilized in combination with scintillators and photo-detectors in the MINOS and MINERvA neutrino experiments, as well as other particle physics experiments. K27 is used to shift scintillator light to a higher wavelength. As shown in the figure, it primarily emits light with a wavelength between

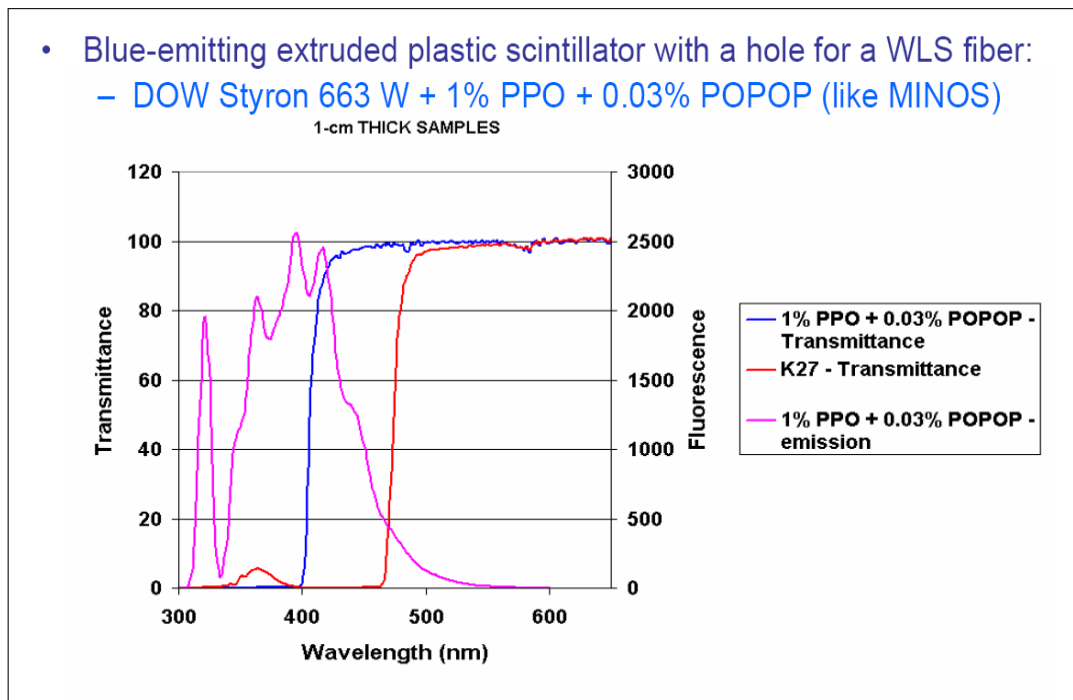


Figure 15: Polystyrene and K27 Dopant Transmittance Characteristics[3]

470-500nm, which corresponds to a much higher PDE in our SiPMs, hence if utilized properly it would serve as a suitable solution to our optical matching. In our lab, we had large stock of 1mm and 1.2mm diameter green WLS fibers. Using these fibers, we devised a plan to make a connector between our scintillator and the face of our SiPM array, thus shifting the wavelength accordingly. Figure 16 below depicts the basic structure of the wavelength shifter. On the left hand side we have the EVB/SiPM combination. To the right of that we have a component which connects the face of the SiPM to the face of the main shifter component. To the right of that, we have the third component, which couples the main shifter component to the front end of the scintillator, which is seen on the far right.

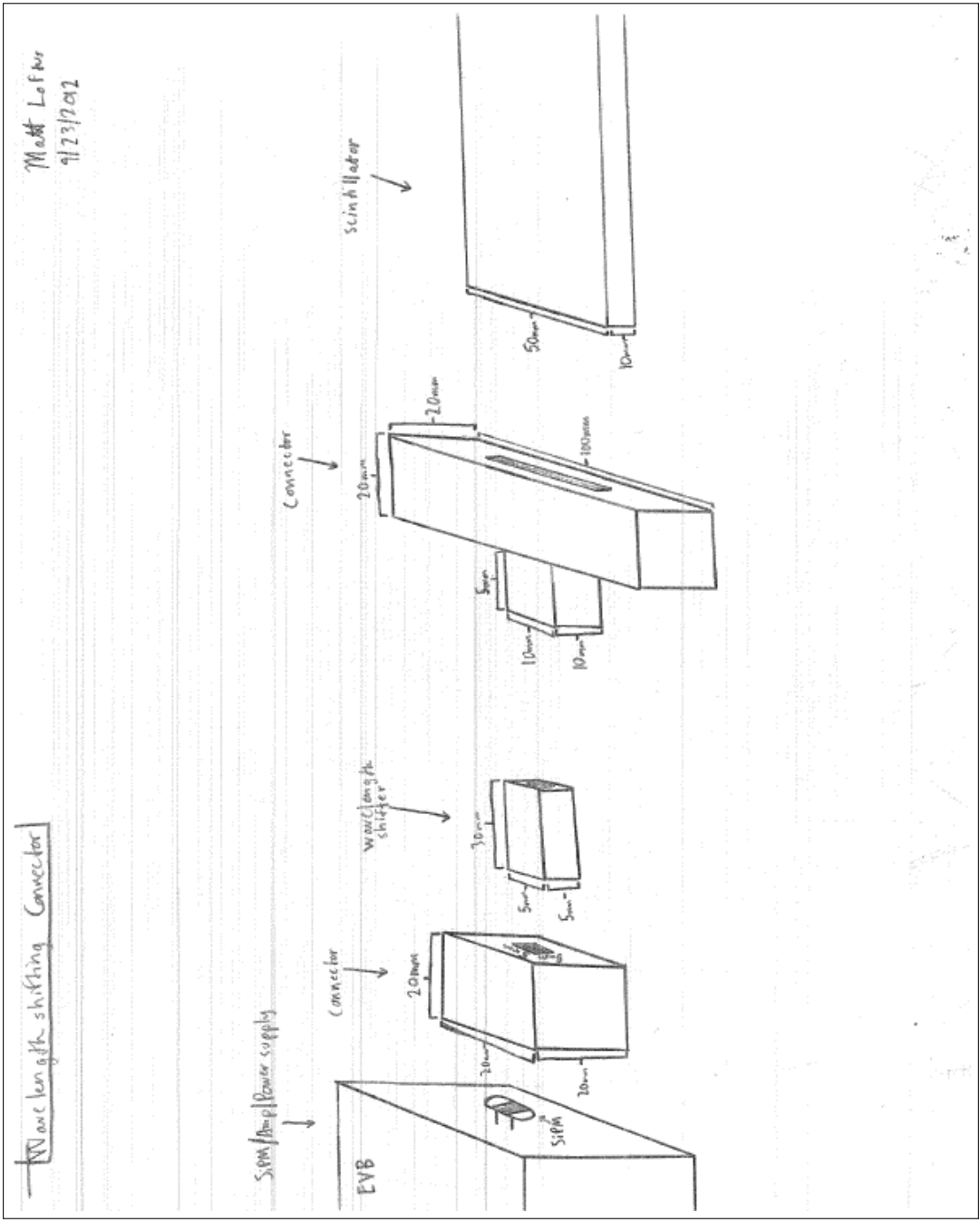


Figure 16: Wavelength Shifter Overview

Figure 17 shows each of the connector components in much greater depth with accurate dimensions. We note the 9 circular holes in the device on the left hand side. This is the component of the shifter where the ultra-violet light is absorbed and re-emitted in the green portion of the EM spectrum, performing the main function of the connector. Here 9 WLS fibers, each 30mm in length, are strung through the connector and each one secured in place using epoxy resin. Our fibers were initially over a meter long, so we had to find an efficient method of cutting them and polishing such that we would not significantly reduce the transmission. To do this, I initially cut the fibers with a razor blade, but this created cracks in the fibers, damaging their output and rendering them useless. To solve this and ensure the fibers maintained their integrity, I heated the razor blade for approximately 20 seconds with a propane torch, immediately before cutting. Using the heated blade I was able to cut through the fibers without creating any cracks. After cutting, I coated each of the fibers in epoxy resin and strung them through the connector individually until all 9 were in place. After letting the epoxy cure for 24 hours, I proceeded to cut the excess fiber ends off of each side of the connector, again with a heated razor blade. I then polished each end slowly using a series of fine grit polishing sheets. Using a progressively higher grit each time, I was able to achieve a smooth finish, where each side had a high degree of transparency and minimal surface scratching, as viewed through a magnifying lens. The other portions of figure 17 depict the front-end and back-end parts of the connector, respectively. The dimensions of these components had to be accurate to a single millimeter for the correct faces to align and to ensure that the enclosure was still light-tight.

I worked in collaboration with machine shop technicians, and had them fabricate all of the individual pieces. We had to make a number of changes and iterations of the initial design based on the precision and types of equipment available for metalworking. I have summarized the necessary modifications in figures 18 and 19.

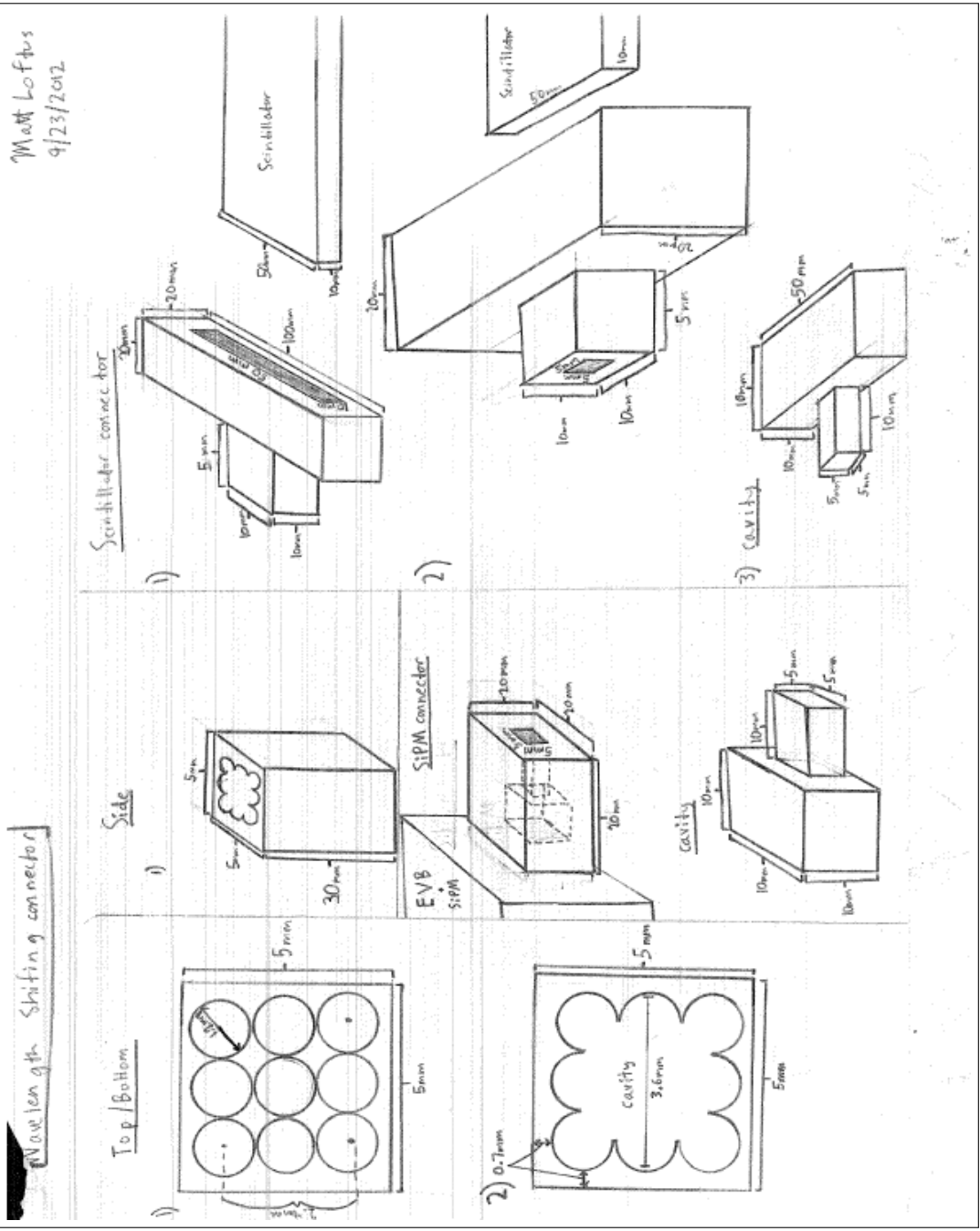


Figure 17: Smaller components in depth

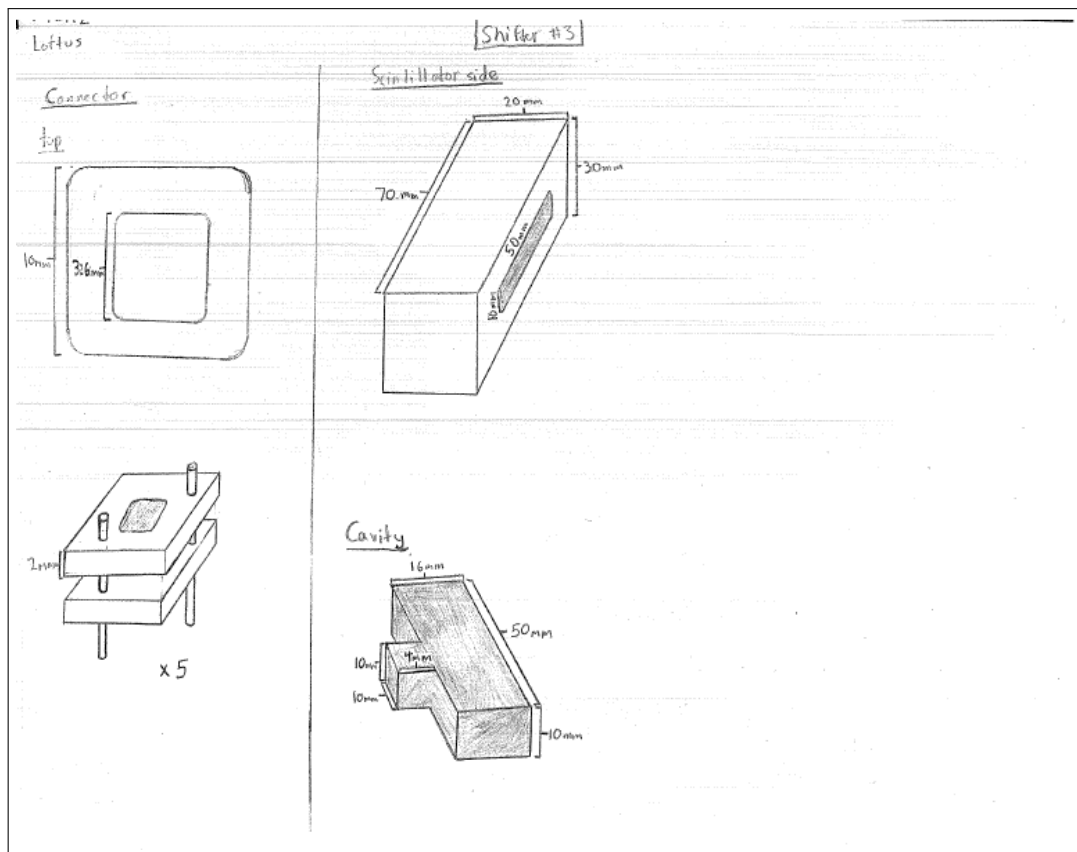


Figure 18: Main wavelength shifting component redesign

Ultimately, the final design was significantly different component-wise than the original, but all of our original specifications and functions were still met. The procedure of putting the actual connector together involved a slow process of binding each metal piece together with epoxy, allowing it to cure, then proceeding to bind those components together and repeating the process until the apparatus was complete. Once the apparatus was in one solid piece, I applied RTV caulk to the gaps and locations where different components met to ensure it was light-tight. In regards to the scintillator, I applied 3 coats of titanium-dioxide paint to the clear surfaces of the polystyrene, leaving exposed only the roughly 3mm×3mm square meant to mate with the end of the fiber-optic connector. On top of this layer of paint I added an additional layer of the reflective sheet mentioned previously, to ensure no light escaped from the back end or the non-couple portion of the front end. To actually join the two surfaces, I applied a thin film of Bicon BC-630 optical grease to the end of each face (to minimize reflection losses), inserted the scintillator into the slot lined up with the fiber-optic face, and sealed them with RTV

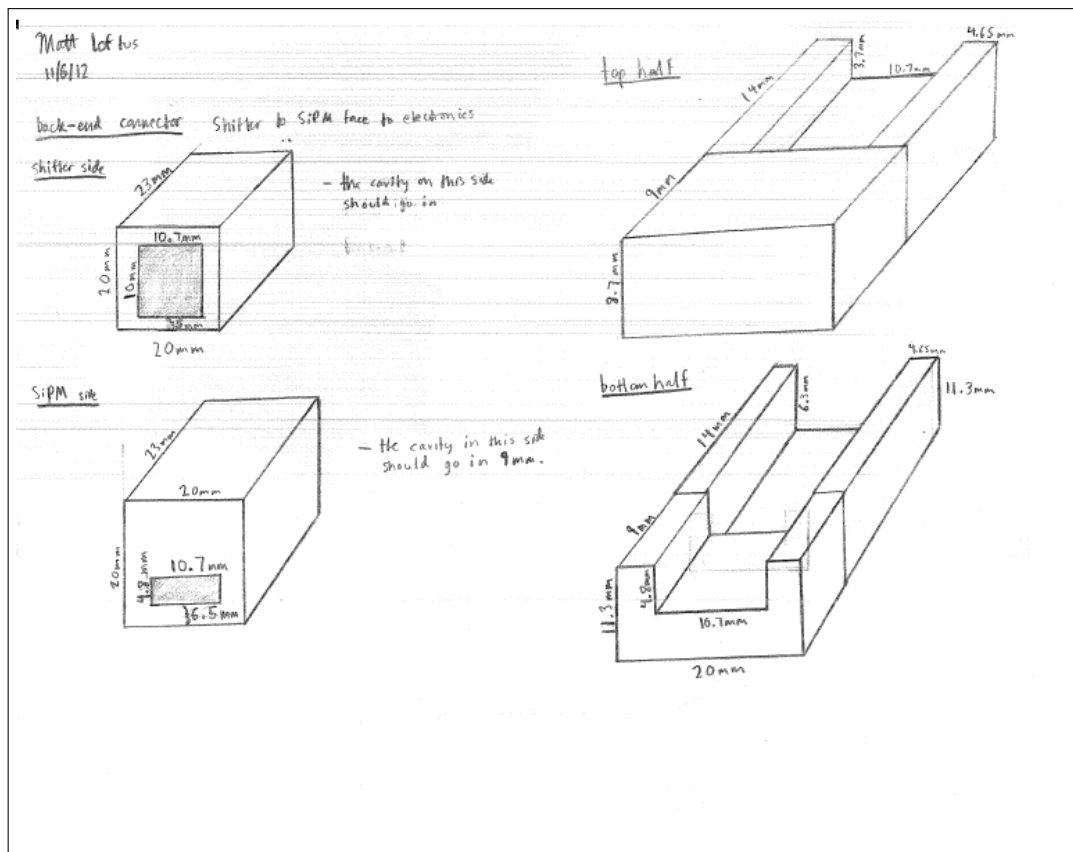


Figure 19: SiPM/Shifter side connector

caulk. For the connector on the opposing end, I used a 4-lead rectangular connector to extend the leads of the SiPM. I then inserted the SiPM into the connector, such that its face was flush against the fiber-optic connector, again using the same technique of applying a thin layer of optical grease at the interface between the two. Lastly I sealed the front end portion with RTV, and placed the assembled shifter in the braces of the TOF counter. The final product in its 80-20 mounting apparatus in the dark box is shown in figure 20.

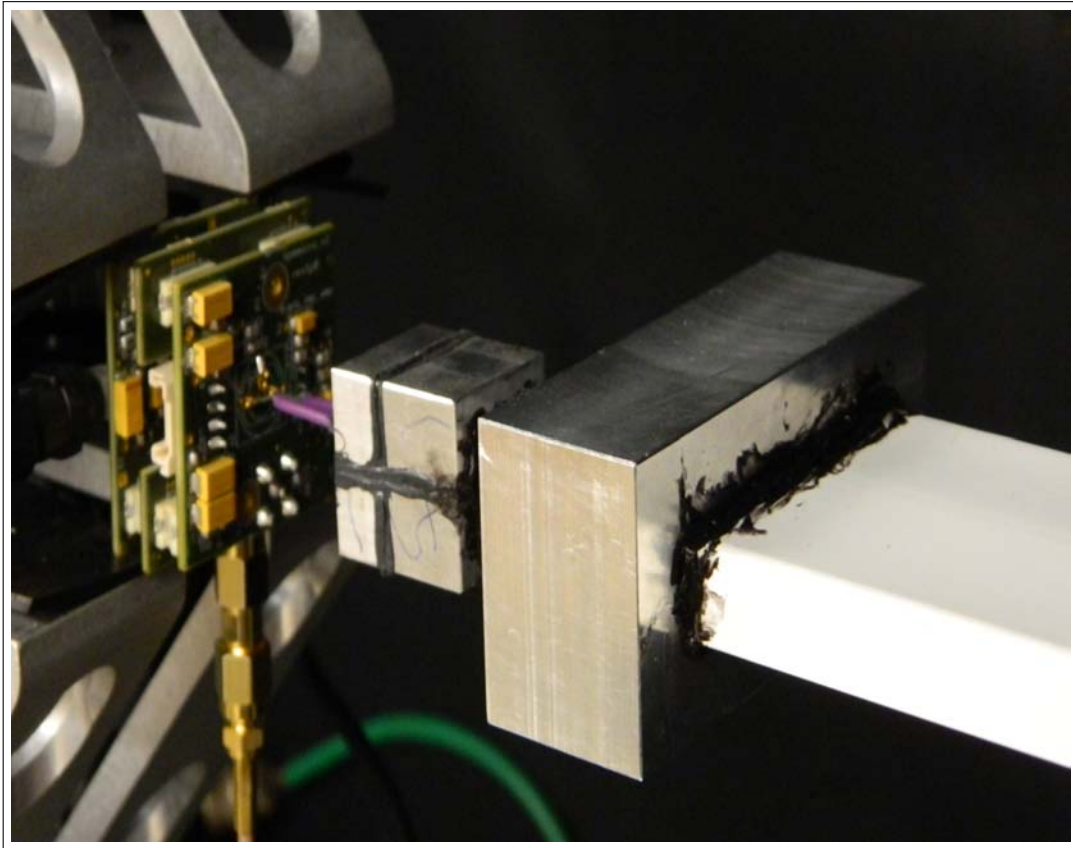


Figure 20: Scintillator/SiPM pair with wavelength shifting connector

5 Performance Analysis: SiPM/Scintillator Output and Integrated Charge Spectra

5.1 Premise

Following the construction of our wavelength shifter, we needed to develop a method to study the performance of our different SiPM/Scintillator coupling methods and determine which would yield the best performance in our time of flight counter. The four cases we had were SiPM with no scintillator, SiPM/scintillator directly coupled (surface-to-surface), SiPM/scintillator with optical grease at the interface, and lastly our wavelength shifter coupling. To study each of the methods, we decided to compare them with the output of the SiPM on its own. Observing the voltage traces and corresponding amplitudes was useful, but as the pulses lasted typically over 100ns, the amplitude was not completely informative of the SiPMs output. To take this into account, we also integrated each voltage trace and recorded the values in a histogram to

get a spectrum of integrated charges, yielding a more complete understanding of the events in our detector. We note that here we were studying the performance of a single counter, as opposed to our coincidence rate tests, which involved the use of a pair of counters. Hence for each case, we set up one scintillator with the appropriate coupling method and recorded the results.

5.2 Voltage Traces and Spectra

Using our 1mm 10050 SiPM array, with the voltage bias set to 30.05 Volts, we took the following traces. In our voltage traces, we set the scope persistence parameter to 20 seconds, which means the scope displayed all of the traces that had been taken in the previous 20 seconds, beneath the most recent trace. This setting is valuable because it allows us to distinguish the peaks corresponding to the the number of incident photoelectrons and study the general behavior over time, rather than studying each individual pulse. Significant outliers may not appear in the final scope trace, but their values are recorded into the integrated charge histogram. Also, we set the scope to trigger on signals less than or equal to -10mV, on the negative edge of those signals.

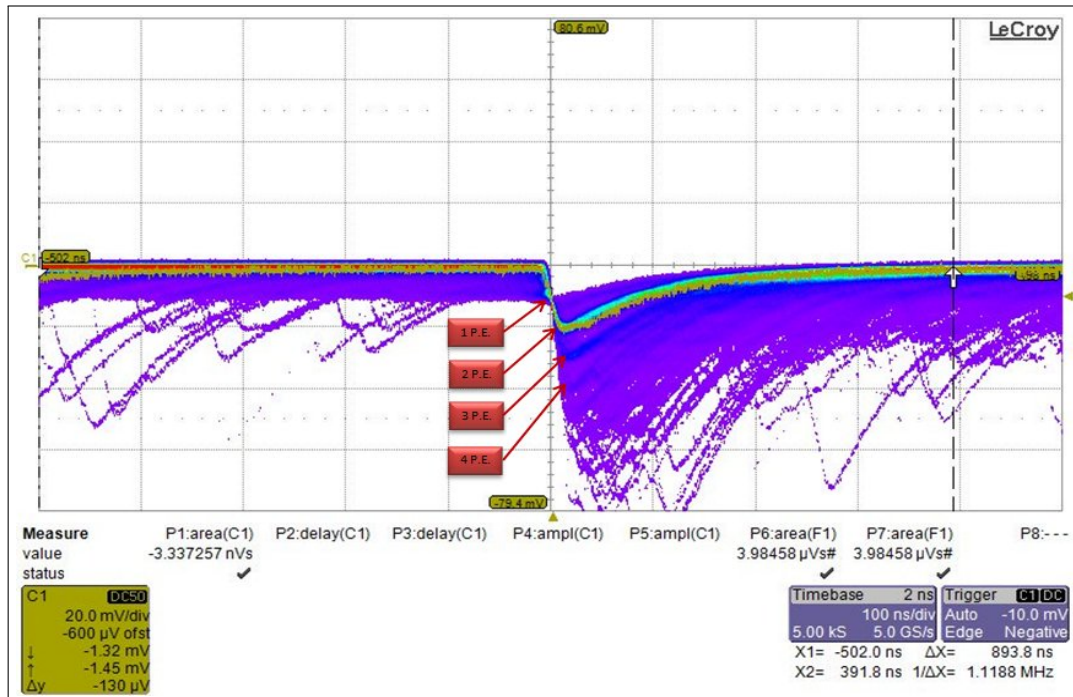


Figure 21: SiPM w/out Scintillator Voltage Output

In figure 21 we see our 1 P.E., 2 P.E., etc. peaks well defined on the trace, with blue lines surrounded by a purple background. The different peaks correspond to the number of photoelectrons generated in the SiPM for a single event. More energetic events, MIPs for example, can create multiple photoelectron pulses. As a MIP can create more scintillation light, it may cause a higher number of pixels in the SiPM array to fire. When multiple pixels fire, we get a larger signal amplitude above the 1 P.E. level. Here the highest common events appeared to take place at the -80mV level.

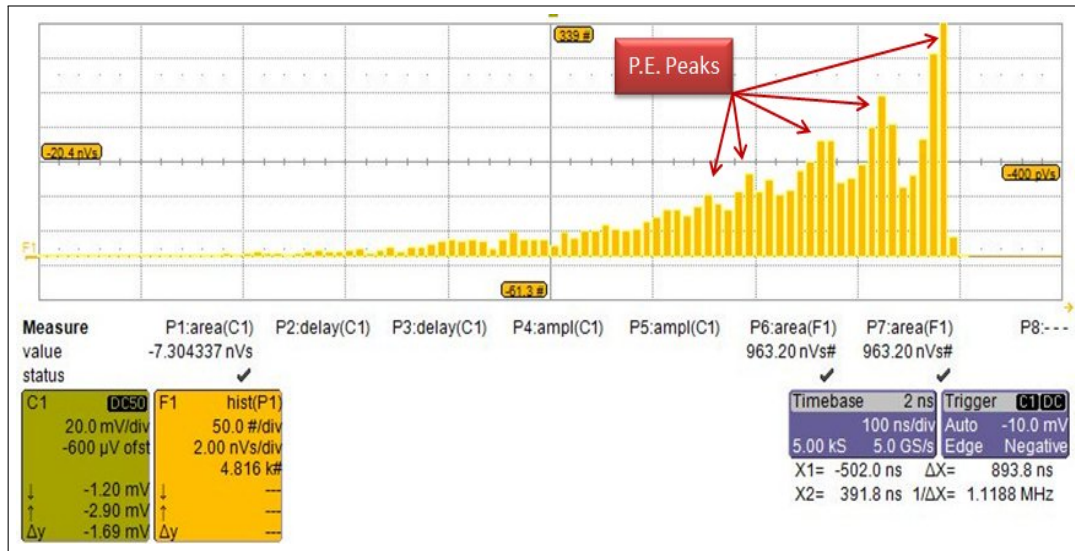


Figure 22: SiPM w/out Scintillator Integrated Charge Spectrum

In figure 22 we see the peaks corresponding the number of incident photoelectrons, as observed in the voltage traces. These peaks are well defined, with 1 p.e. \sim -2.8nVs, 2 p.e. \sim -2.96nVs, and 3 p.e. \sim -5.18nVs.

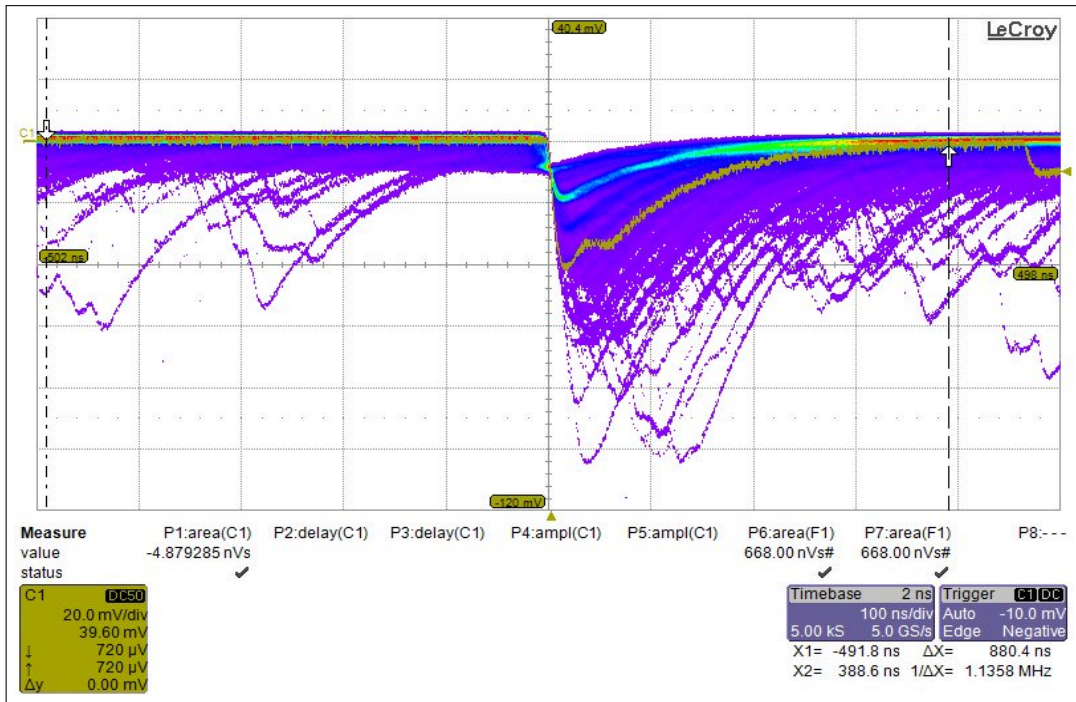


Figure 23: SiPM/Scintillator Direct Couple Voltage Output

From figure 23 we see the photo electron peaks well-defined. For the most part the highest common events were again at $\approx -80\text{mV}$, however we do see some events in the 100mV range. We note that the persistence setting on the voltage traces causes them to display all the traces of the previous 20 seconds, and automatically deletes the traces prior to that. This setting is constantly running on the scope, so we are always seeing what has occurred in the last 20 seconds. Hence the high amplitudes of some of the pulses in figure 23 could simply be due to the random occurrence of events and the particular 20 second time interval the scope was displaying.

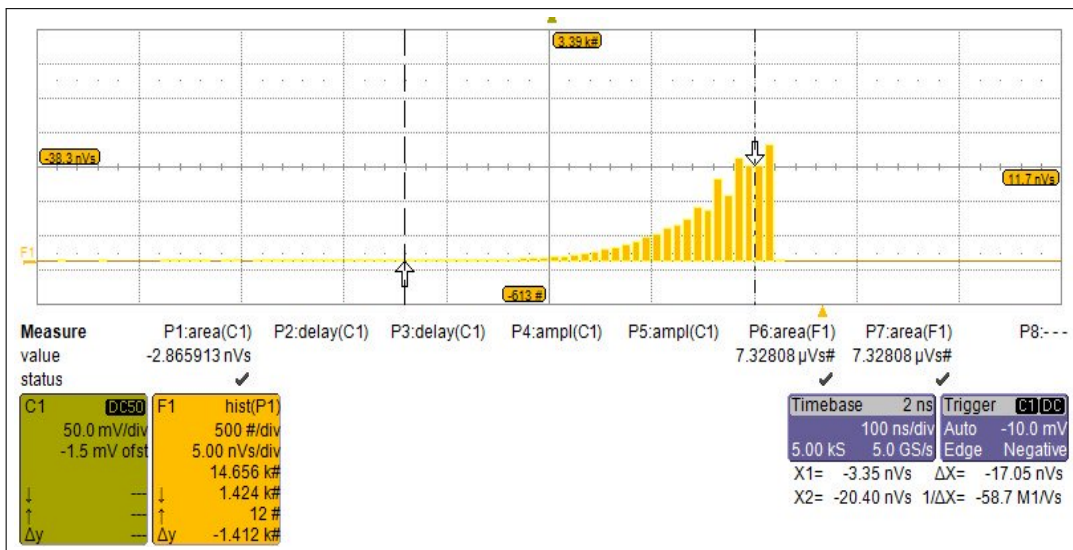


Figure 24: SiPM/Scintillator Direct Couple Integrated Charge Spectrum

We see from figure 24 the P.E. peaks are less defined, with more events having integrated charge values between the levels at which the P.E. peaks occur. However, we note that the scale of this histogram is larger, and thus the bin value as well, than the previous histogram. Hence the lack of definition is likely due to the fact that we are viewing a horizontally 'compressed' version of the histogram in figure 22.

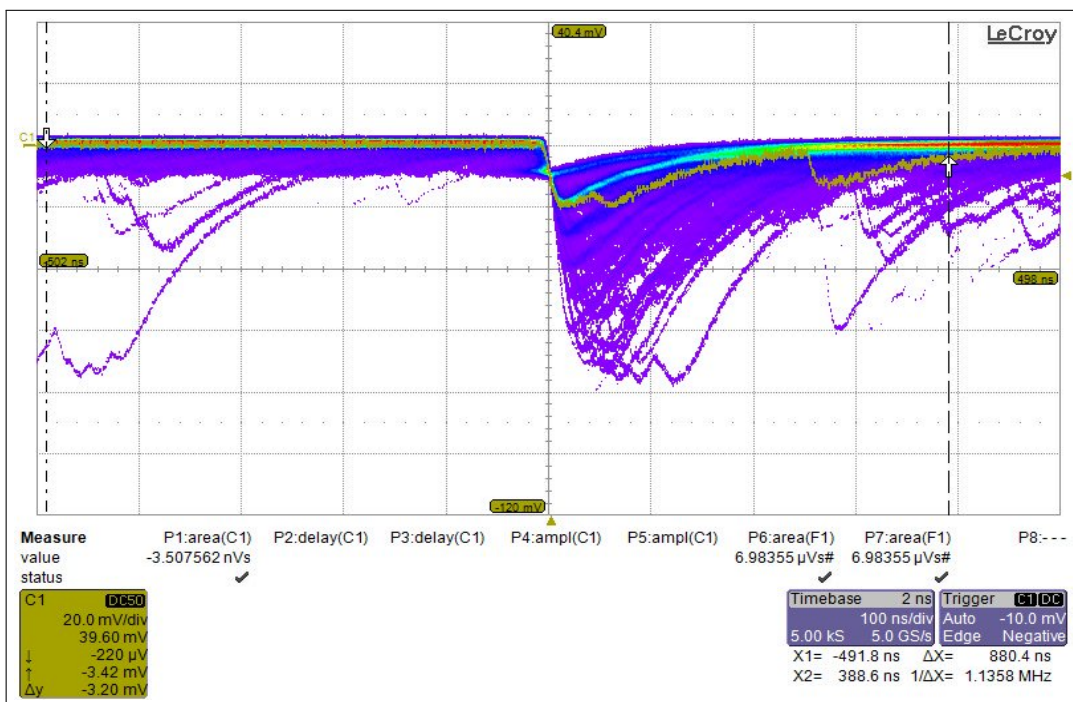


Figure 25: SiPM/Scintillator Optical Grease Voltage Output

For the optical grease coupling, the voltage trace results were quite similar to the those of the first two cases, with the peaks well defined, as shown in figure 25.

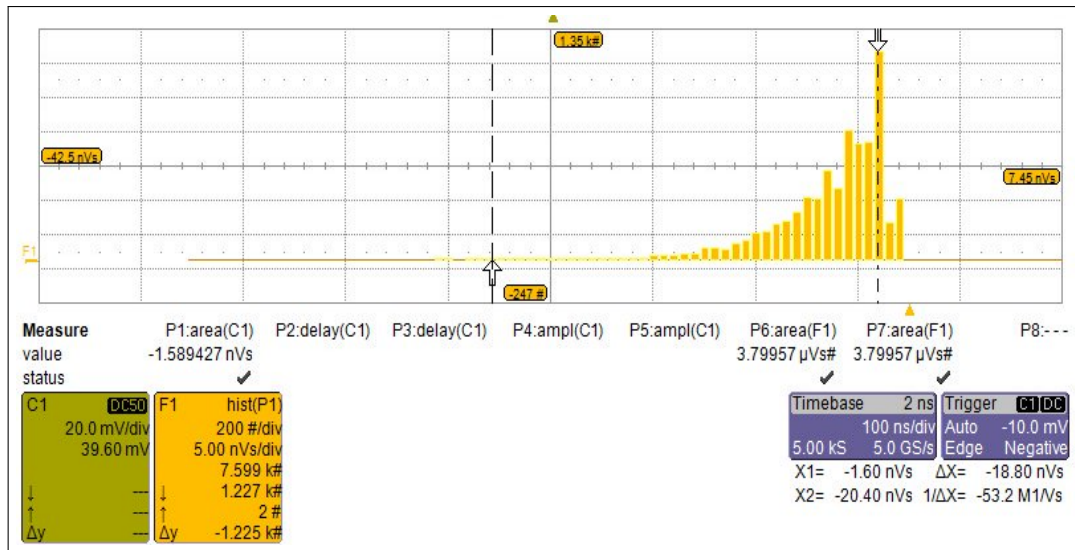


Figure 26: SiPM/Scintillator Optical Grease Integrated Charge Spectrum

For the optical grease coupling, the integrated charge spectrum, shown in figure 26 was very similar to that of the direct-couple case, with the P.E. peaks not clearly defined.

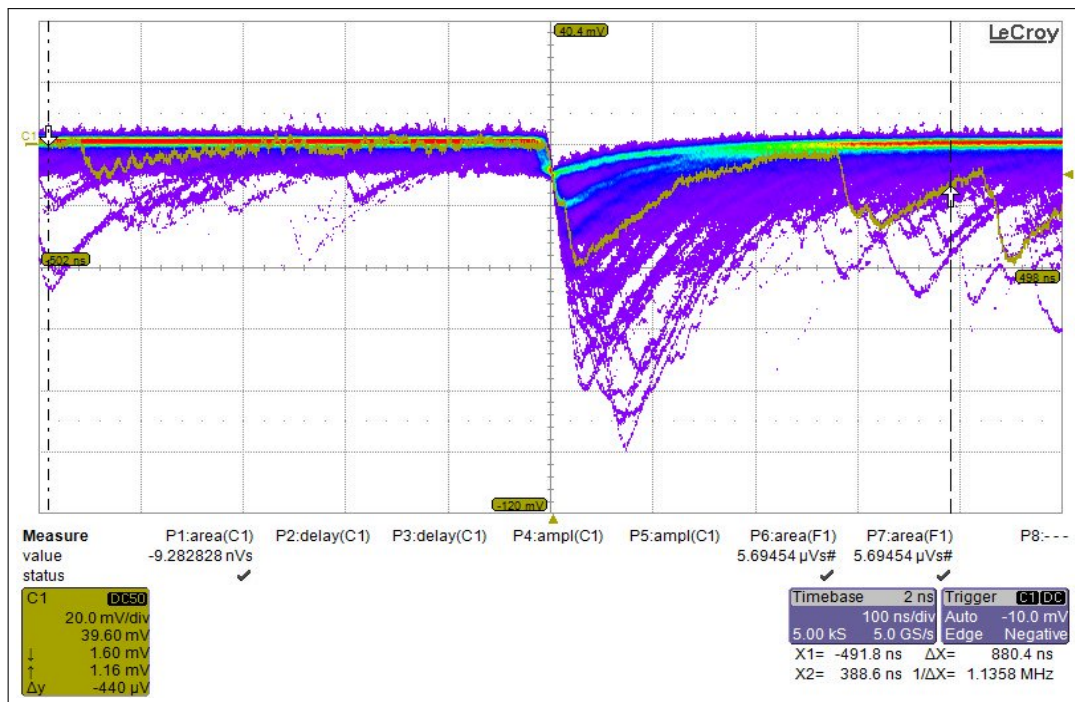


Figure 27: SiPM/Scintillator Wavelength Shifter Voltage Output

For the wavelength shifter case, the voltage amplitudes were in a similar range as those of the first three cases, however the P.E. peaks are not as clearly defined in the voltage scope trace as in the other cases. Also, there is an extra element of noise in the voltage traces, causing most of the individual signals the jitter up and down over the course of each acquisition. This could be due to the wires used to couple the SiPM to the EVB. We note that in the wavelength shifter, as we connected the SiPM leads into a rectangular connector, we had to insert two more leads on the opposite side in order to couple the SiPM to the EVB. The EVB contacts for the SiPM, however, are thinner than most common single strand wire. As a result of this I was forced to unravel multi-strand wires, clip off unwanted strands, then recoil them to produce wires with a diameter small enough to fit the EVB. The termination of these individual strands may have let to reflections and other deficiencies which contributed to the noise.

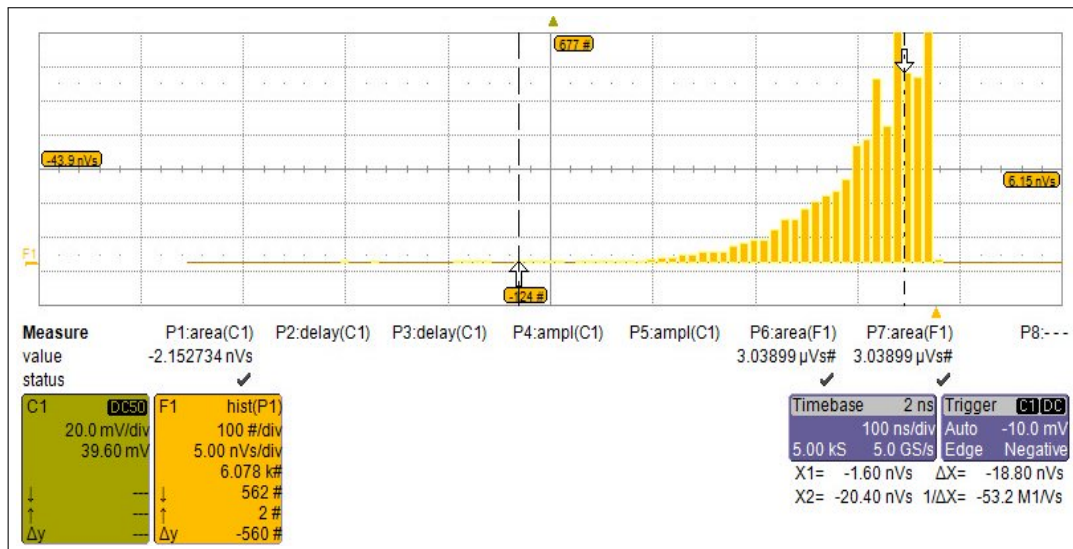


Figure 28: SiPM/Scintillator Wavelength Shifter Integrated Charge Spectrum

From figure 28, we see the integrated charge spectrum was similar to that of the direct-couple and optical grease cases, again with the P.E. peaks not well-defined. From this analysis of the different coupling methods we were able to see that they all shared similar voltage output amplitudes, and we were able to discern the different P.E. peak resolutions from the integrated charge spectra. This visual inspection was useful, but it did not lead us to applicable results about the different coupling methods.

5.3 Analysis: Taking SiPM Dark Activity(no Scintillator present) into Account

To gain useful data about our different coupling methods, we needed a procedure to separate the data produced by the SiPM independent of the coupling method, from the data which was actually due to the presence of the scintillator. In other words we wanted to know how many events were actually caused by the scintillator, and what those events were like. From the scope, we were able to take the histogram data (bin location(V.s) and bin population(#events)), and export it to a spreadsheet. Now as the SiPM produces negative output voltages, the more negative integrated charge values actually correspond to the more energetic events. What we wanted was a way to measure the occurrence of high level events in the SiPM benchmark case, and compare it to that of the other coupling methods. To do this we created a plot where the x-axis value corresponds to the integrated charge value, whereas the y-axis value corresponds to the percentage of the total events that had an integrated charge value less than the current x value. Hence for each integrated charge value, it would show what proportion of the total events had a higher (absolute) integrated charge than that value. In our tests we set the voltage bias to 30.58 Volts, and ran the histogram function for 5 minutes for each of the coupling methods. Also we set the threshold of the oscilloscope trigger to -20mV up from -10mV. This was out of concern for the effects of noise and low level events on the operation of the oscilloscope. The scope has an inherent dead time after a trigger occurs in which it cannot acquire data. Our concern was that at a threshold of -10mV, we would experience an extremely large quantity of low amplitude events, and thus more total dead time, hindering our ability to detect the high amplitude events we were looking for.

The plot of figure 29 gives the percentage relationship described above. We note the general trend of the plot; that the proportion of total events with a higher magnitude decreases as the integrated charge decreases. In this case, we were interested in using the 1% level as a benchmark. Though the plots detail does not show the precise location of the 1% mark, our data showed that it occurred at $-2.45 * 10^{-8}$ Vs, and that there were 94 total events with an integrated charge greater than $-2.45 * 10^{-8}$ Vs. In the absence of high amplitude noise, if we subtract the number of high level events in

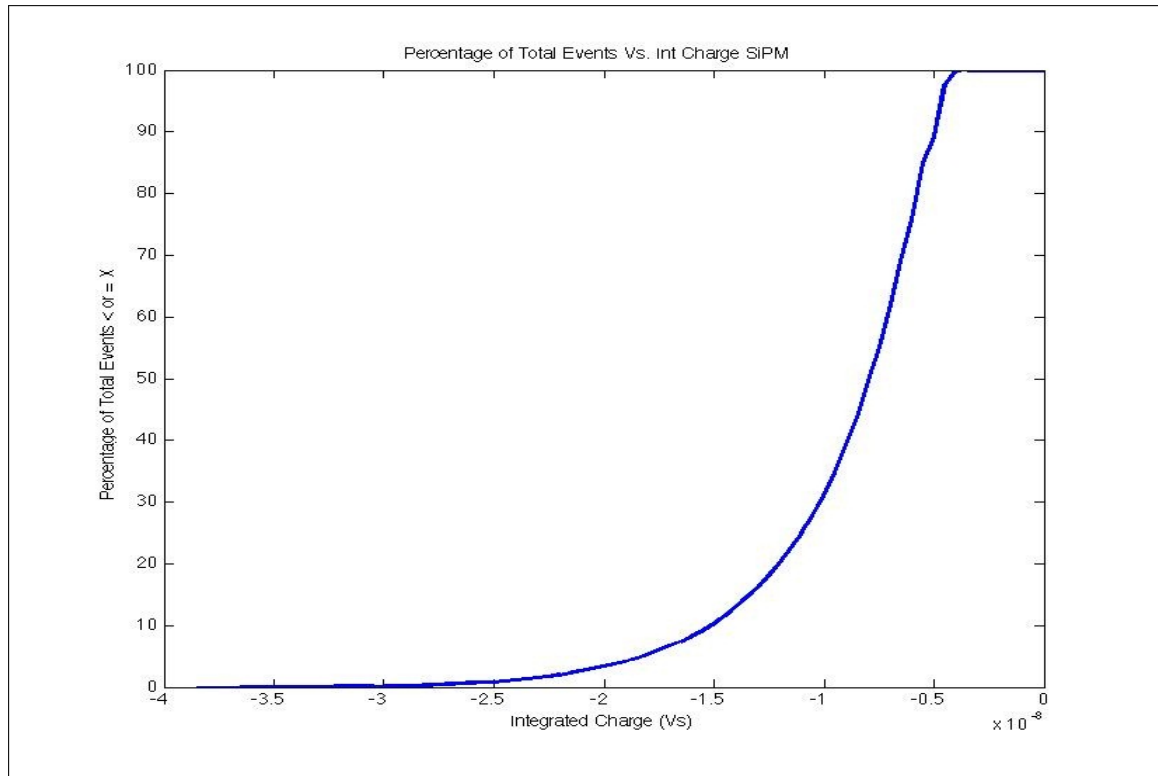


Figure 29: SiPM w/out Scintillator Percentage Plot

the SiPM benchmark case from that in one of our scintillator coupling cases, we would yield the number of true MIP events. Hence taking similar histograms for the three coupling methods, we yielded the following values. For the direct-couple, we yielded 111 events of magnitude greater than $-2.45 \times 10^{-8}Vs$, which gives us 17 real MIP events. Now for the other cases, though, we found zero events above the $-2.45 \times 10^{-8}Vs$ level. Taking into account our previously mentioned vertical MIP rate of 65 muons/minute, we would expect 325 muons to pass through our scintillator in 5 minutes. Now we know the histogram function has a limit on the percentage of events it can record, so we would not expect to see all of those events. Even so, the number of high level events we detected was a surprise, perhaps resulting from our coupling methods, or from our data acquisition methods and the instruments used, which may not have been optimally suited to record cosmic events.

We repeated a similar test the following week, extending some of the parameters to gain a better understanding of the underlying issues. We set the voltage bias to 29.5 Volts, which is the recommended operating voltage given by the SensL data sheet. We

also kept the trigger level at -20mV. For this test, we ran each case for 20 min to increase the number of total events and thus the corresponding error. Also, instead of just using the 1% level, we looked at events above the 1.1%, 5.3%, 11.2%, 21.6%, and the 47.2% levels, to see if the behavior we observed in the last test extended to the entire integrated charge spectrum. We chose those decimal values because of the discrete nature of the bin location given by the scope, i.e. because we are unable to find the number of events for an integrated charge value located between two bins. Ultimately, we found for each coupling method, for each percentage value just mentioned, the number of events was less than that of the SiPM benchmark case. This showed that in the dark box, with no additional light source, the integrated charge spectra for each of the different coupling methods had a smaller magnitude than that of the SiPM benchmark case. This did not make sense, and led us to seek new means of studying the scintillators responsiveness to light.

6 Radioactive Source Test

In light of the problems we faced with our different coupling methods and detecting MIP events, we wanted to test the scintillator with an energetic source of charged particles to ensure that it was in fact working and that the scintillator was increasing the output voltages detected by our SiPM. We also wanted to observe whether or not the counting rate of the SiPM increased with the introduction of a radioactive source. For this we used a Cobalt-60 radioactive pellet. The Co-60 is a Beta emitter, which emits photons of 1.173MeV and 1.333MeV [9]. In this test we coupled the scintillator to the 10050 SiPM with optical grease, set the trigger to -20mV, and ran the histogram for 20 minutes so that we could compare the integrated charge spectrum to that of the optical grease coupling case from the previous experiment.

Figure 30 depicts the number of total events above each particular integrated charge value with and without the radiation source present. The difference between the two curves shows the total number of events that we can attribute to the presence of the Co-60 source. We saw that a radiation source did in fact yield more high-level events,

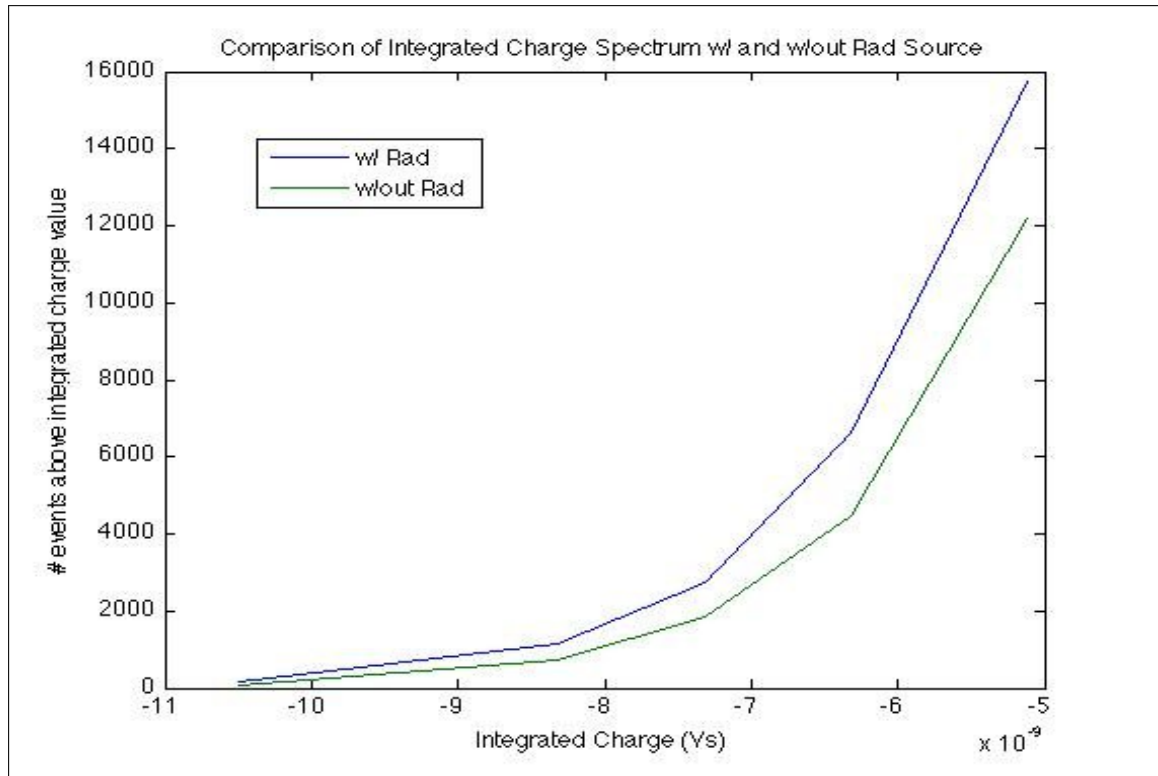


Figure 30: Radioactive Source Test Results

and that the integrated charge spectra of our SiPM/Scintillator combination increased. This result was valuable, as it showed that our system was responsive to radiation.

7 Counter Efficiency: PMT Based Tests

7.1 Overview

With an understanding of how our different coupling methods and varying amounts of radiation affected the output of our system, we sought to find a new measure of the efficiency of our counter, in this case relative to a pair of preexisting counter known to be operational. For this we used two photomultiplier tubes, each coupled to a scintillator/light guide combination, with the light guide acting to direct the scintillation light to the photocathode of the PMT. Figure 31 shows the structure of our initial test setup for our efficiency measurements.

In figure 31, the two cylindrical objects are the PMT housings, which contain the voltage biasing elements as well as the PMTs themselves. On the right hand side of

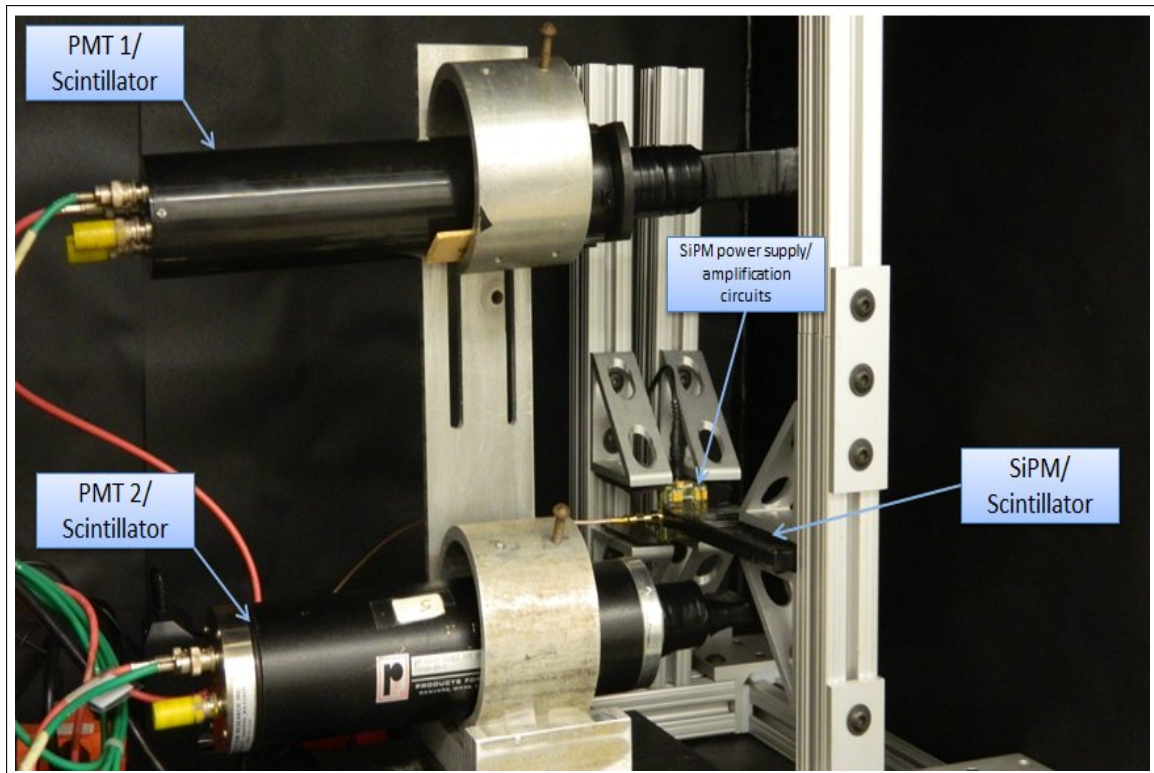


Figure 31: Initial Efficiency Test Setup

the PMT housings, we see a smaller black cylindrical object followed by a rectangular object. The cylindrical objects are the light guides, while the rectangular pieces are the scintillators. In between the two PMT elements we see another rectangular piece of scintillator coupled to a green circuit board, both secured with the vertical clamps. This is the SiPM-scintillator counter element whose efficiency we are studying. The idea is based on the nature of vertical muons. If a muon traveling downwards strikes both PMT based counters, it must inevitably travel through the SiPM based counter in between the two. The way we measure the efficiency is to count the number of coincidences in the two PMT based counters and compare it to the number of coincidences we get in all three counters. We will refer to a coincidence in the two PMTs as a double coincidence, and a coincidence in the two PMTs and the SiPM as a triple coincidence.

Figure 32 shows a typical double coincidence from one of our subsequent tests. In the oscilloscope trace, we see the three different traces corresponding to channels 1,2 and 3. Here PMT 1 is the yellow trace on channel 1, PMT 2 is the pink trace shown on channel 2, and the SiPM is the dark blue trace shown on channel 3. The light blue

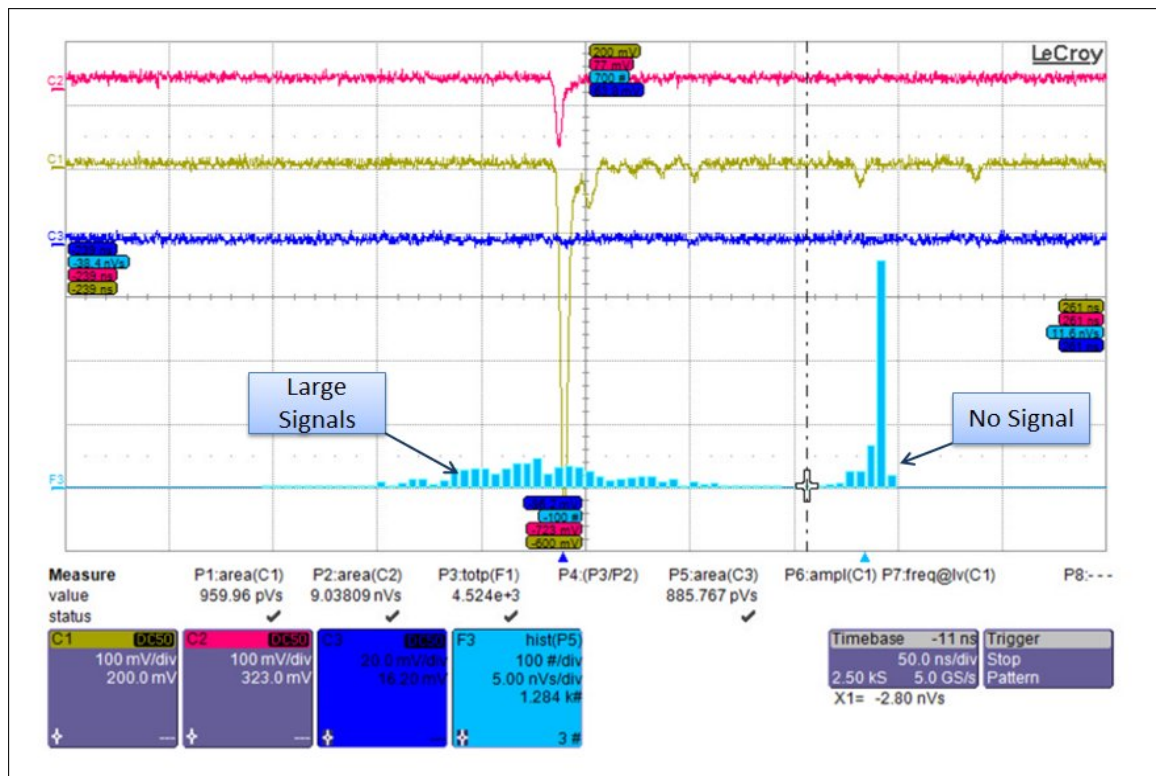


Figure 32: Typical Double Coincidence

histogram at the bottom records the integrated charge of the SiPM trace taken at each trigger of the scope. Noting that each horizontal division corresponds to 50ns, we see in this example that PMT 1 and PMT 2 received strong signals at essentially the same time, while the SiPM output no signal. An important aspect to note of these tests was the special pattern on which we triggered our oscilloscope. Here we would get a scope trigger each time CH1(PMT 1), and CH2(PMT 2) went below -50.0mV at the same time, regardless of amplitude of the SiPM signal. We see the results of this in the histogram in the bottom of figure 32, where 2 large PMT signals and no SiPM signal resulted in histogram values in the 'No Signal' region, while triple coincidences with large SiPM signal amplitudes resulted in large histogram values in the 'Large Signals' region. The significance of this is that if we take the ratio of the total number of histogram events in the 'Large Signals' region to the total number of histogram events, we have an measure of the efficiency independent of the measurements taken with our NIM modules. Hence this allowed us to check the operation of our NIM efficiency tests, ensuring that the two independently measured efficiencies agreed, in addition giving us a more quantitative

data about the SiPM's response to a real triple coincidence.

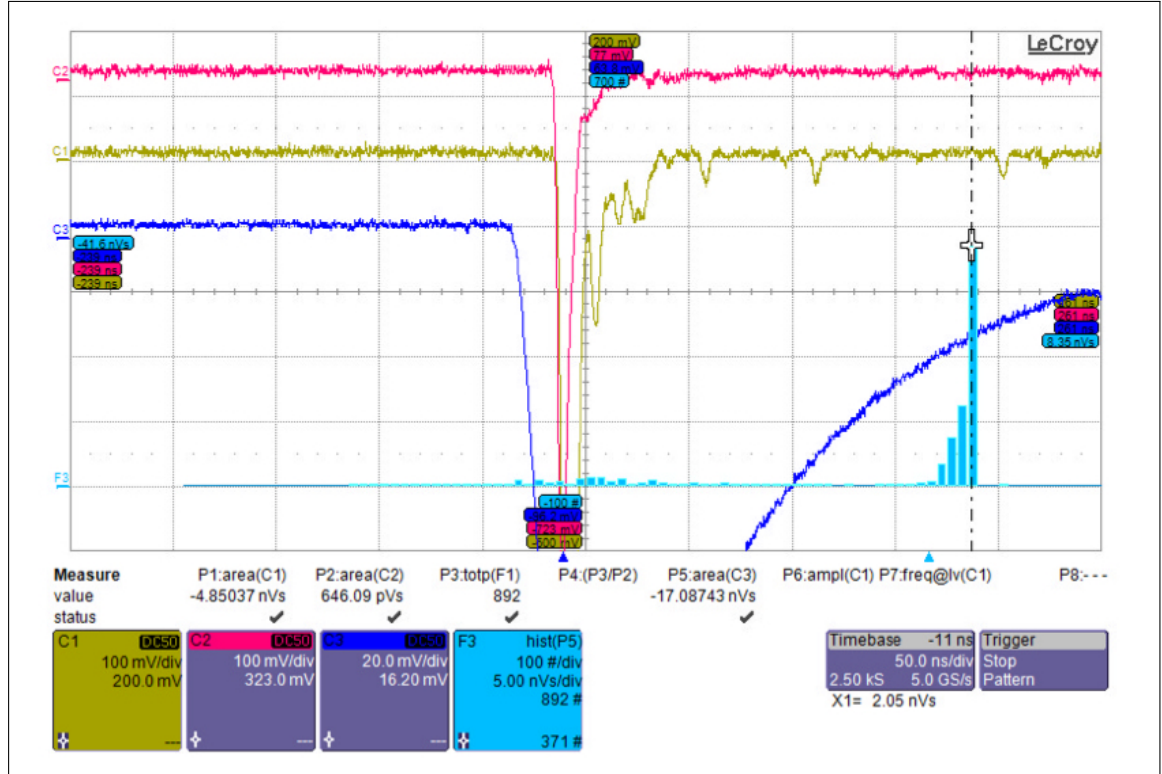


Figure 33: Large-Amplitude Triple Coincidence

Figure 33, however, shows a triple coincidence with very high signal amplitudes. Here we see large amplitude signals occurring in all 3 of the detector elements simultaneously. We must point out that the vertical scale for the PMT traces is 100mV/division, while that of the SiPM is 20mV/division, so in reality the SiPM signal is much smaller than that of the PMT. We note that the SiPM signal shape is different than that of the PMTs and that it exceeds the scope window, but it is evident that the 3 events peaks occur within a few nanoseconds of each other. If the SiPM based counter operates perfectly, we would expect to get a significant event in the SiPM every time we get a double coincidence, thus giving us the same number of double and triple coincidences. If however, our SiPM based counter is not very efficient, we would expect the number of triple coincidences to be less than the number of double coincidences. The efficiency is determined by the ratio of triple coincidences to double coincidences.

$$\epsilon = \frac{\# \text{Triple Coincidences}}{\# \text{Double Coincidences}} \times 100 \quad (5)$$

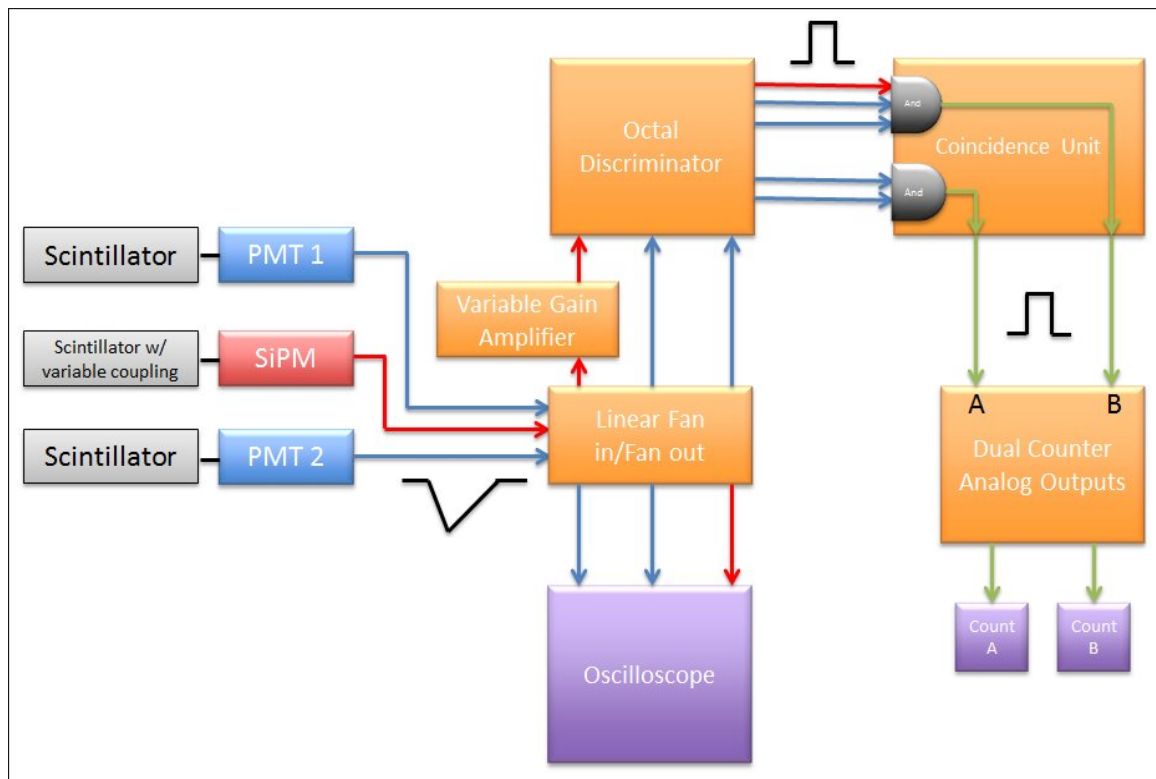


Figure 34: NIM Logic Efficiency Measurement Setup

Where ϵ denotes the efficiency as a percentage. The logic for our setup is similar to that of our previous coincidence rate measurements from section 3, with some key differences. The basic logic and setup of the NIM electronics units is shown in figure 34.

In the diagram we show all the electrical connections from the photo-detectors to the final count recording. The PMTs signals are shown with the blue lines, while the SiPM signals are displayed in red. Tracing the paths of the signals, we see the PMT signals are fed to an analog fan-in/fan-out unit, which mirrors the signals to multiple locations. This unit is used because when splitting a signal via 2-output/1-input cable connectors, the amplitude of the signal is decreased as a result. This unit, however, outputs multiple copies of the input signal, each with the same amplitude as the input. From the fan out, we send our PMT signals to an oscilloscope for viewing and to the discriminator. As described previously, the discriminator outputs a logic signal if the input signal amplitude is above a certain preset threshold. From the discriminator, we then send the PMT signals to the coincidence unit, which will output a logic signal if the input signals overlap in time. In figure 34, the operation of this unit is shown by

the AND gate located at the input. Finally, the coincidence output is recorded by a dual counter, which records the number of coincidences that occur. The SiPM signal follows a similar path except for a brief detour through an amplification unit. We do this because the SiPM signals are smaller than that of the PMTs, and often lower than the minimum threshold we can set in the discriminator, so we must amplify its signal before it is passed to the discriminator. The main counting operation can be seen between the discriminator and coincidence units. From one output we have the two PMT signals sent to one input channel of the coincidence unit, measuring the number of double coincidences. From the other output we send the two PMT signals as well as the SiPM signal to the second input channel of the coincidence unit, measuring the number of triple coincidences. Using this setup we were able to measure the efficiency for multiple coupling methods, for multiple settings of the NIM parameters.

Prior to performing our efficiency tests, we wanted an understanding of the event rates of each of the detector elements and the role false/random coincidences would play in our measurements. Using similar methods as in the previous coincidence test, we were able to measure each of these event rates. They are given in table 1:

Detector Element	Rate(Hz)
PMT 1	32.10
PMT 2	11.67
PMT 1+PMT 2	0.02
SiPM WLS	1.42×10^5
SiPM Optical Grease	1.47×10^5

Table 1: Detector Element Rates

7.2 Efficiency: Geometry 1

For our first efficiency tests we used the setup shown in figure 31 above, which we will refer to as geometry 1. In this case we coupled our scintillator to our SiPM with optical grease. We adjusted the voltage bias on the SiPM to 29.5 volts, 2 volts above the breakdown voltage according to the data sheet. We set each discriminator output pulse to have a width of 45ns, and set the thresholds of the three discriminator channels to -50mV. For the SiPM this translated to an actual threshold of -5.0mV due to the x10

amplification process. Running the test for 46 hours and 32 minutes, we recorded 4931 double coincidences and 2411 triple coincidences, corresponding to $\epsilon = 48.89\%$.

Now upon observing the scope trace of our SiPM at this bias voltage and coupling, we noted that the 1 p.e. threshold was at -7mV approximately. This meant that in our first test, events below the 1 p.e. level, which were mostly due to noise, were contributing to the number of triple coincidences we got. This gave us an misleadingly high efficiency. Subsequently, for the next test we raised the threshold on D_3 to -70mV , corresponding to a new threshold of -7mV for the SiPM. This would effectively remove much of the noise level events present in the previous case. Again we used the optical grease to couple our scintillator with the SiPM. In this test, after 18 hours and 5 minutes, we recorded 1112 double coincidences and 365 triple coincidences, corresponding to $\epsilon = 32.82\%$. This efficiency was lower than that of the -5mV threshold, which agrees with our expectations of removing noise level events. By the same measure, a larger proportion of these coincidences were likely real coincidences.

Switching coupling methods, we next coupled the scintillator to the SiPM with a wavelength shifting fiber, with a thin layer of optical grease between the fiber end and the SiPM array. For this we strung the fiber through a new piece of the same type of scintillator, but we did not glue it in place. We light-tighted the scintillator and added reflective material to all light exit points except for the small area where the fiber end rested. As as the fiber diameter and SiPM array dimensions were the same size; 1mm, this required a perfect coupling of the two. In this regard the optical grease layer, though not permanent, was essential in securing the fiber end in the right place. Now, after running this test for 18 hours and 14 minutes, we recorded 1114 double coincidences and 379 triple coincidences, corresponding to $\epsilon = 34.02\%$.

The conclusions we drew from the first set of efficiency tests were that in our initial geometry, the counting efficiency saw no measurable changes when we implemented the WLS fiber. Another important realization was that in this setup, there existed areas of overlap between the two PMT scintillator pieces where no portion of the SiPM-scintillator filled the area in between the two. In other words, the setup was such that a muon traveling vertically downwards(or slightly angled) could pass through

the two PMT detector elements without ever hitting the SiPM element. Also, the concern arose that scintillation may actually occur in the light guides, which are nominally non-scintillating or low scintillating optical conductors between the scintillator and the PMT. This would increase the negative area of overlap described above. In fact, all of these factors detracted from the overall efficiency of our SiPM detector, and we sought to solve these problems in the subsequent experiments.

7.3 Efficiency: Geometry 2

Following the results of our previous experiment, we reoriented the positions of the two PMTs in relation to the SiPM-scintillator element, seeking to specifically restrict the vertical overlap of the two PMTs to areas which contained the SiPM-scintillator in between. To do this we angled the two PMTs, the top PMT with approximately a 45 degree clockwise rotation, and the bottom with an approximately 45 degree counter-clockwise rotation. This reduced the vertical overlap of the light guides and other parts of the scintillators. The setup can be seen in figure 35, which we will call geometry 2.

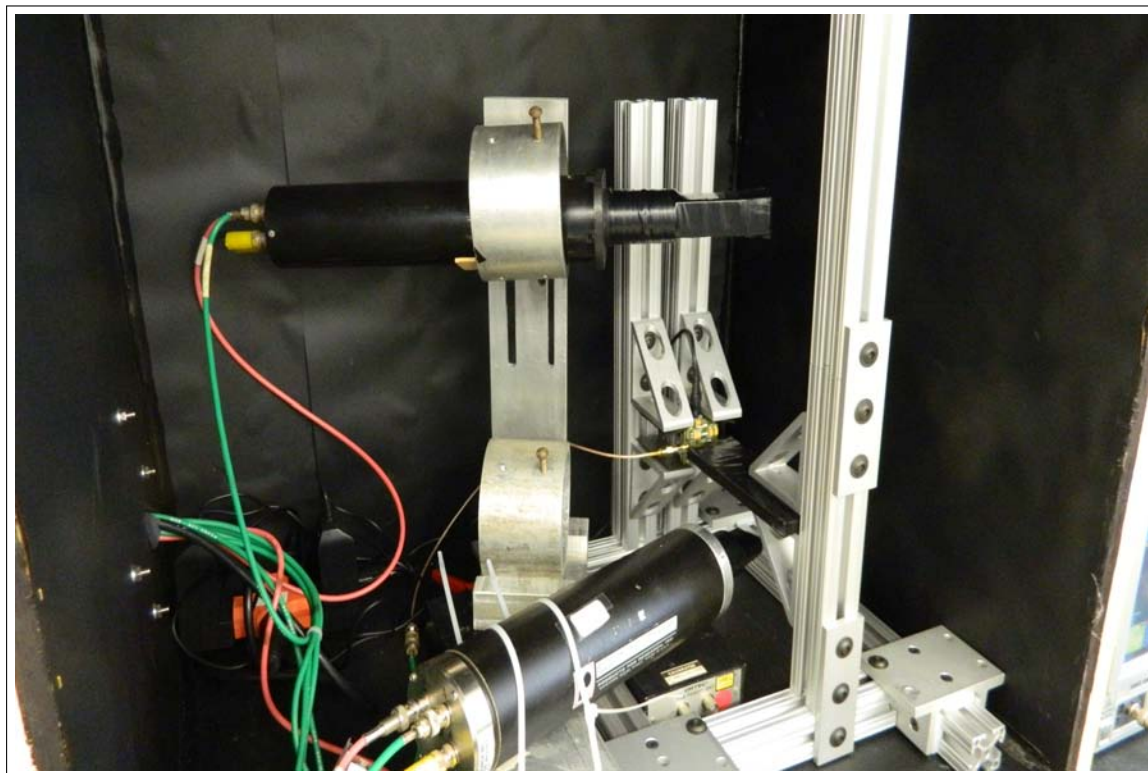


Figure 35: Efficiency Setup: New Geometry

For this geometry, we conducted an efficiency test with the SiPM coupled to the scintillator with the WLS fiber, at an SiPM threshold of -7mV, as before. After 12 hours and 33 minutes, we recorded 1107 double coincidences and 288 triple coincidences, giving us $\epsilon = 26.01\%$. Although at first glance we believed we had improved the orientation of the PMTs, but here we saw our efficiency was actually less than that of geometry 1 in the WLS case. We are uncertain of the exact cause of this decrease in efficiency, but one conclusion might be that we actually increased the amount of PMT-scintillator overlap which we were seeking to decrease.

With a basic structure of our efficiency experiments established, we sought to investigate the rate of false coincidences in our current setup. The motivation was similar to that of our false rate studies of section 3.1, with the understanding that because each discriminator output a pulse of nonzero width, there was inherently a chance that the 3 discriminator pulses would overlap despite the events being out of time, hence creating a false coincidence. Now for a triple coincidence to occur, the SiPM would have to fire a discriminator pulse as a double coincidence between the two PMTs was occurring. As we know the values of the two discriminator output pulse widths for the two PMTs, we know that the maximum time interval in which a double coincidence can occur is when the end of one discriminator pulse overlaps with the beginning of the second discriminator pulse. By that logic, we see that the maximum interval in which this can occur is simply the sum of the two pulse widths.

$$\text{Max Interval}_{\text{Double Coincidence}} = \text{PW}_{D_1, \text{PMT } 1} + \text{PW}_{D_2, \text{PMT } 2} \quad (6)$$

Where the PW on the right hand side corresponds to the two discriminator pulse widths in question. Now if we take into account the rate of the discriminator output corresponding to the SiPM, we yield a formula for the fractional amount of false coincidences that will occur.

$$\text{FC}_{\text{Fractional}} = \text{Max Interval}_{\text{Double Coincidence}} \times \text{Rate}_{D_3, \text{SiPM}} \quad (7)$$

Where $\text{FC}_{\text{Fractional}}$ is our fractional amount of false coincidences, and the quan-

tities on the right are the variables described above. Now we know the pulse width of both PMT discriminator pulses to be 46.6ns. Taking into account our SiPM rate given in table 1, we yield

$$FC_{\text{Fractional}} = 0.013$$

With an expected value for the amount of false coincidences occurring, we sought to experimentally determine the amount of false coincidences and compare it with our expected value. To do this, we introduced a time delay to the discriminator output pulse corresponding to the SiPM, such that when a triple coincidence occurred the third pulse would be out of time with respect to the other two. Hence our counter would not register a count when an actual triple coincidence occurred. The only way for the counter to actually register a value would be if the SiPM discriminator pulse occurred before the discriminator pulses of a double coincidence. As these would be out of time, we see that this would be a false coincidence. Hence the channel of our counter recording triple coincidences would actually now correspond to a total count of false triple coincidences, while the other channel would still correspond to the real count of double coincidences. The logical elements for this are shown in figure 36, with count A corresponding to the real count of double coincidences and count B corresponding to the total number of false triple coincidences.

An example of what occurs when we get a real coincidence in this test setup is shown in figure 37. In this oscilloscope trace, we see clearly that a real triple coincidence has occurred. The green square wave corresponds to the delayed discriminator output of the SiPM. We see that it is delayed approximately 80ns from the time of the coincidence. We cannot see the discriminator pulses of the PMTs due to the 4-channel maximum of the oscilloscope, but from previous tests, we know they occur within a few nanoseconds of the actual coincidence, hence the effective delay of our SiPM discriminator signal is between 70-80ns. As our PMT discriminator pulses are 46.6ns wide, we see that none of our real triple coincidences will be recorded by the counter.

After running this test for 18 hours and 38 minutes for the WLS coupling, we recorded 844 double coincidences and 10 false coincidences, corresponding to a fractional false triple coincidence rate of 0.012. This was very close to our expected value,

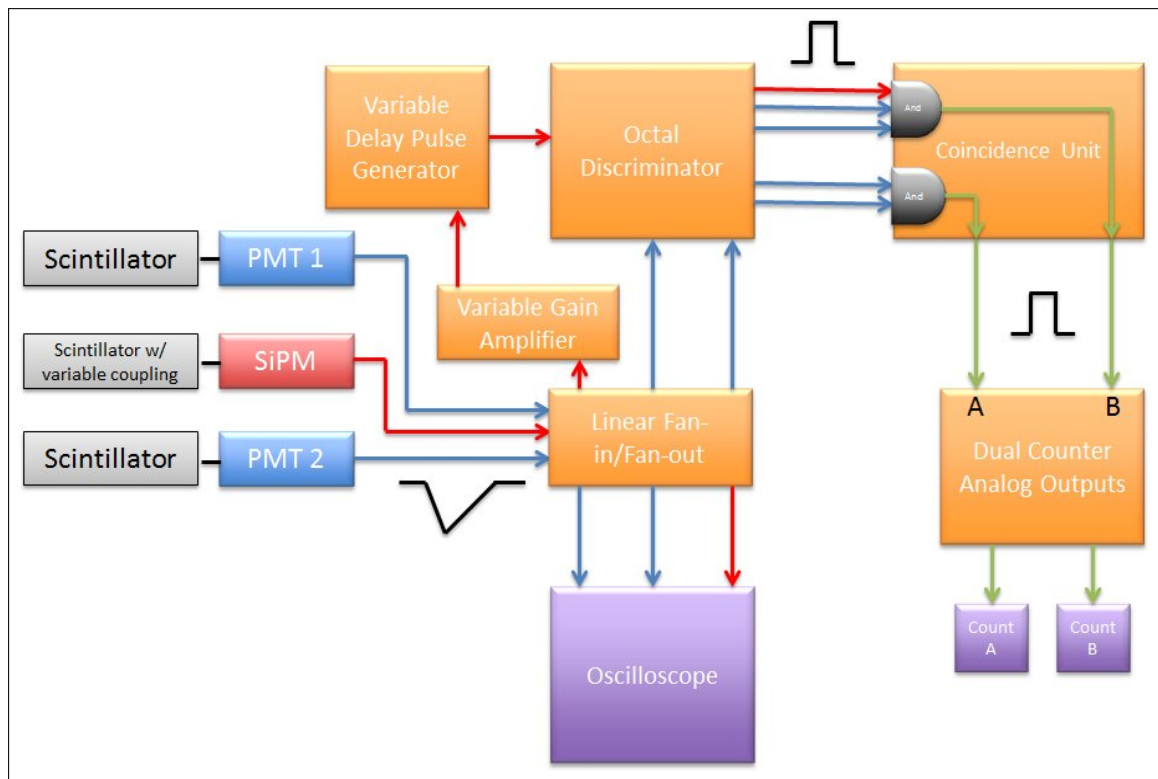


Figure 36: False Coincidence Test Logical Elements

and helped to validate our procedure for determining the expected value. Ultimately, geometry 2 yielded a lower efficiency for the WLS coupling than geometry 1. We were unsure of the exact cause of this, but were still led to believe it may have been caused by the SiPM-scintillator not covering some of the area where double coincidences occurred.

7.4 Efficiency: Geometry 3

Following our first two detector geometries, we sought to reorient the detector element such that there would be no areas where double coincidences could occur without SiPM-scintillator occupying the space between. The final iteration of our detector geometry, geometry 3, is shown in figure 38.

Here we see the orientation is close to optimal, and we confirmed with straight edges that there were no areas of PMT-scintillator overlap which did not contain the SiPM scintillator in between. Now, with the new setup we proceeded with a few experiments. First, we conducted an efficiency test with the WLS coupling on the SiPM, at a threshold of -7mV , as before. After 24 hours and 40 minutes, we counted 1563 double

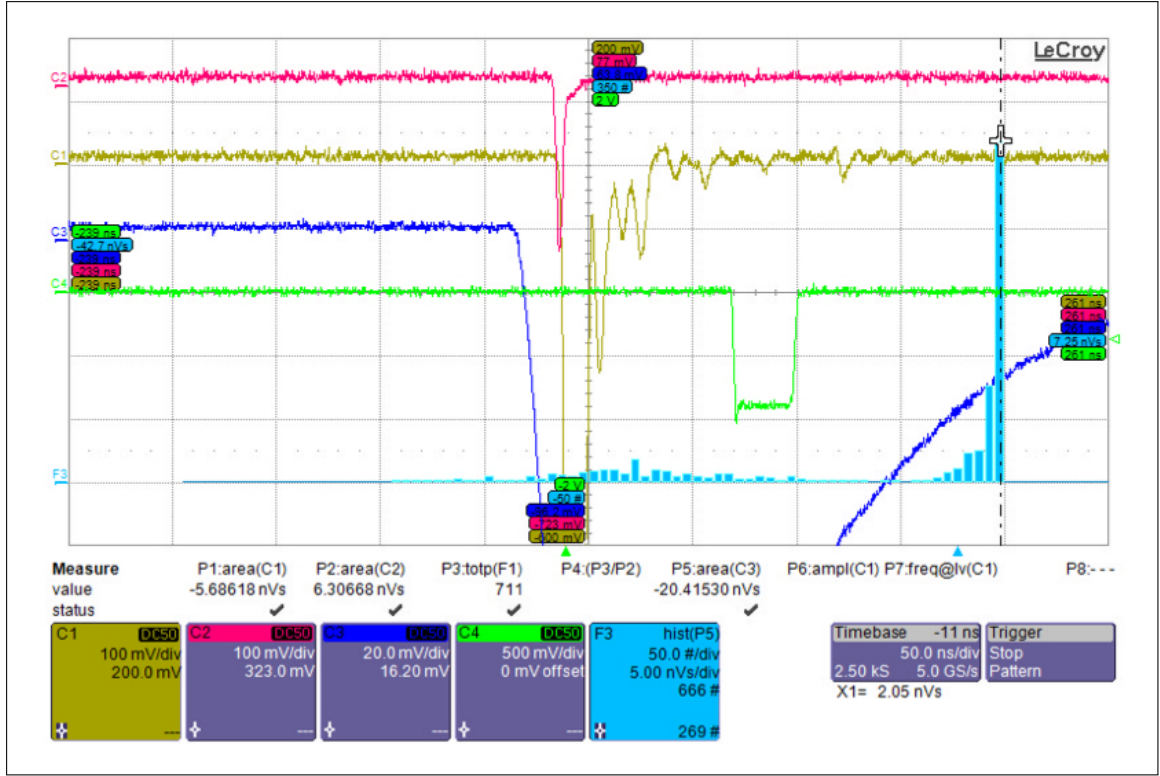


Figure 37: False Coincidence Oscilloscope Example

coincidences and 912 triple coincidences, corresponding to an efficiency $\epsilon = 58.34\%$. This was by far our best efficiency.

Following this, we conducted a false coincidence rate test on the same exact setup. After 8 hours and 17 minutes, we recorded 544 double coincidences and 13 false coincidences, giving us a fraction false coincidence rate of 0.024. While this differs from our expected value of $FC_{\text{Fractional}} = 0.013$, the difference is not very large.

For a complete understanding, we then conducted an efficiency and false coincidence rate test for the case of SiPM-scintillator directly coupled with optical grease. We conducted these tests with the SiPM threshold at -7mV , as with the other cases. After 11 hours and 55 minutes, we counted 643 double coincidences and 153 triple coincidences, yielding an efficiency of $\epsilon = 23.79\%$. This efficiency was actually lower than that of geometry 1, which is surprising based on the overlapping area argument described above as a source of inefficiency.

For the false coincidence rate study, we had to use the rate of the SiPM with the optical grease coupling to determine our expected fractional false coincidence rate.

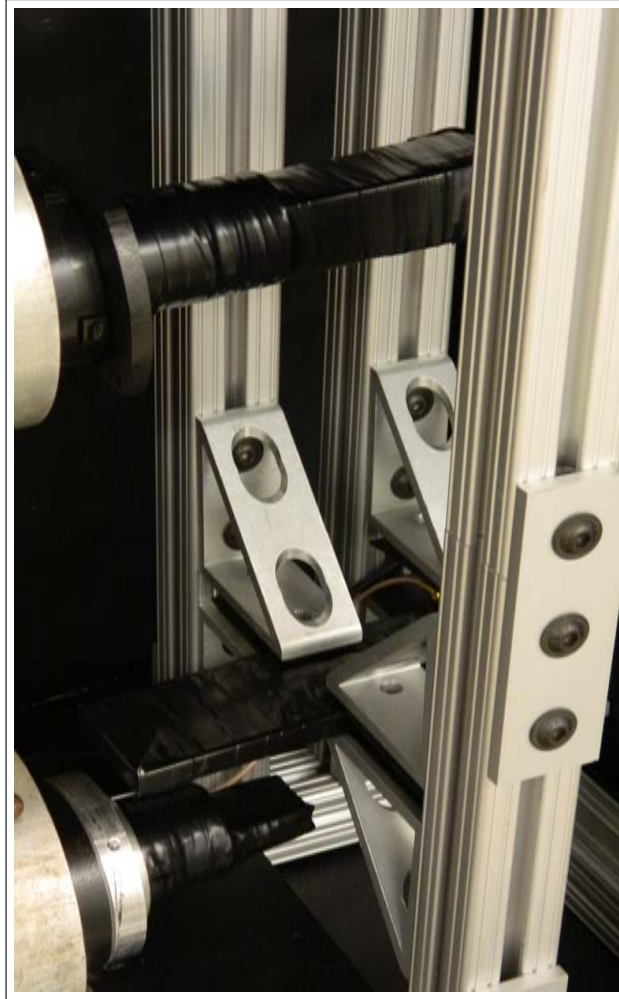


Figure 38: Efficiency Test Setup: Geometry 3

Taking the appropriate rate from table 1, the same maximum time interval as before, and solving equation 7, we yield:

$$FC_{\text{Fractional}} = 0.014$$

Now running our false coincidence test for 2 hours and 26 minutes, we yielded 221 double coincidences and 0 false coincidences. This result is low, but does not differ greatly from our expected rate. Regardless, the efficiency of the optical grease coupling in geometry 3 was significantly less than that of the WLS coupling.

8 Conclusions

In our study of SiPMs' performance as the photo-detector element of scintillator radiation detectors, we learned a number of concrete things. Overall, we have two main

cases to consider: our scintillator directly coupled to an SiPM using optical grease, and our scintillator coupled to an SiPM using a combination of a wavelength shifting fiber in combination with optical grease. Our initial coincidence rate experiments utilizing 2 SiPMs seemed to show that our counters were inefficient, but in retrospect the use of two different kinds of SiPM, among other factors, may have greatly hindered the efficiency of the test setup. In our later counter efficiency tests, we had mixed results, but we determined with a high degree of certainty that the counter with the WLS coupling in the third geometry had the greatest efficiency. The efficiency of that case was markedly higher than that of geometry 1, showing that the improvements in detector orientation led to a direct increase in our counter's efficiency. From the large amplitude of the SiPM signals for triple coincidences, like the example in figure 33, it seems that light collection is not responsible for the inefficiency. If the light yield of the SiPM-scintillator combination was small, that would inevitably lead to a lower efficiency. That not being the case, however, the source of the remaining inefficiency still remains unsolved. Nonetheless, it shows promise that as we improve the geometrical orientation, the efficiency increases.

Regarding the case of directly coupling the scintillator to the SiPM with optical grease, we observed that the efficiency was low for all three of our detector orientations. Though factors such as operating temperature, SiPM array size, and voltage bias may play a role in the efficiency, it seems that the method of direct coupling is not very efficient.

Looking forwards, it would be interesting to implement a wavelength shifting film as a means of coupling the SiPM and scintillator, as that may have a much greater ease of design and implementation. Also, with a larger dark box and more PMT based counters, we could greatly improve our efficiency experiments by adding more PMT-scintillator counters in a more complex geometry. For example using one more PMT and recording the number of triple and quadruple coincidences as opposed to double and triple coincidences. The study reaffirmed the benefits of using wavelength shifting elements in photo-detector-scintillator applications, showing that while perhaps not with direct coupling, SiPMs are viable candidates for large scale detector and HEP experiments.

References

- [1] Devan, Josh. MINERvA Collaboration
- [2] Groupen and Schwartz. *Particle Detectors* 2nd Edition
- [3] Herbert, D.J., D'Ascenzo, N., Belcari, N., Del Guerra, A., Morsani, F., Saveliev, V. *Study of SiPM as a potential photodetector for scintillator readout* Nuclear Instruments and Methods in Physics Research A 567 (2006).
- [4] M.P. De Pascale et al., *J. Geophys. Res.* 98, 3501 (1993)
- [5] Mai, Carsten. *The Tracker of the PERDaiX Experiment*. February 2010
- [6] P.K.F. Grieder, *Cosmic Rays at Earth*. Elsevier Science (2001)
- [7] Pakhlov, P. *SiPM: Development and Applications* (ITEP). Dec 14,2005.
- [8] Para, Adam. *Characterization of MPPC/SiPM/GMAPD's* February 17, 2009.
- [9] Particle Data Group. *Review of Particle Physics*.
- [10] Pla-Damau, Anna. "Blue-emitted extruded plastic scintillator with a hole for WLS fiber." Notes, September 2012
- [11] "MicroSL Silicon Photomultiplier Detectors Datasheet." Rev. 1.3, September, 2011.
- [12] Tesar, Michal. *Scintillator tile and SiPM studies at MPP Munich* CALICE electronics and DAQ and AHCAL main meeting. Hamburg, Germany. December 11, 2012.